Chemical Engineering Journal 535 (2026) 175599

Contents lists available at ScienceDirect

Chemical Engineering Journal

journal homepage: www.elsevier.com/locate/cej

Defect–dopant synergy in graphene/fullerene hybrid nanocomposites with defective and Li-doped defective fullerenes for enhanced hydrogen storage

Yasemin Turhan [a], Betül Duman [a], Mehmet Doğan [a,*], Ersin Yanmaz [b], Zeynep Bicil [a], Berna Koçer Kızılduman [a]

[a] Balikesir University, Faculty of Science and Literature, Department of Chemistry, 10145, Çağış, Balıkesir, Turkey
[b] Balikesir University, Altınoluk Vocational School, Department of Chemical and Chemical Processing Technologies, 10870, Altınoluk, Balıkesir, Turkey

ARTICLE INFO

Keywords:
Fullerene
Graphene
Li-doping
Hybrid nanocomposites
Hydrogen storage
Kinetics

ABSTRACT

This study presents a defect–dopant co-engineering strategy for developing high-performance hydrogen adsorbents based on graphene and its nanocomposites. Pristine C60 was sequentially converted into defective C60 (D—C60) and Li-doped defective C60 (Li-D-C60), followed by hybridization with graphene to construct defect-rich hybrid architectures. Textural analyses revealed Type IV adsorption isotherms with combined micro–mesoporosity, while kinetic modeling confirmed pseudo-second-order behavior ($R^2 > 0.99$). Hydrogen adsorption isotherms were measured in the pressure range of 0–100 bar at 77 K and were best described by the dual-Langmuir model, indicating the presence of two energetically distinct adsorption environments within the hybrid carbon framework. The optimized Graphene-P2.5-Li-D-C60 sample achieved a hydrogen storage capacity of 2.53 wt% at 77 K and 100 bar, exceeding those of pristine graphene (1.81 wt%) and D-C60-based systems (2.17 wt%). Mechanistic analyses indicated a multistep adsorption pathway dominated by boundary-layer diffusion at the initial stage and intraparticle diffusion as equilibrium was approached. This stepwise mechanism, together with defect-induced active site enrichment and Li-driven surface polarization, enhances hydrogen accessibility and adsorption strength. Pearson correlation analysis ($r = 0.50$ for BET surface area and $r = 0.51$ for micropore volume) demonstrates that hydrogen storage performance is governed by the synergistic interplay between porosity, diffusion kinetics, and electronic polarization effects.

1. Introduction

Environmental pollution caused by the combustion of fossil fuels, increasing energy demand, and global climate change pose serious threats to human life. Hydrogen, as a clean and renewable energy source, has been recognized as a promising solution to these challenges. The rapid depletion of fossil fuel reserves and their detrimental environmental impacts have directed scientists toward sustainable energy systems [1]. With its high energy density, zero carbon emissions, and versatile utilization potential, hydrogen is considered one of the most powerful energy carriers of the future [2]. However, its widespread application requires the development of safe, economical, and high-capacity storage methods [3]. Hydrogen storage strategies can be broadly classified into three categories: (i) compression in pressurized tanks, (ii) liquefaction at cryogenic temperatures, and (iii) adsorption on solid materials. The first two approaches are limited by high energy requirements, low efficiency, and safety concerns [4]. Consequently, material-based storage methods have received increasing attention in recent years. Solid adsorbents, owing to their high surface areas, enable hydrogen to be stored through physical or chemical adsorption, offering significant advantages in terms of safety and energy density [5].

Various classes of materials have been investigated for this purpose. Metal–organic frameworks (MOFs) stand out with their exceptionally high surface areas and tunable pore structures [2]. Covalent organic frameworks (COFs), composed of lightweight elements, provide chemically stable porous architectures [6]. Zeolites, with their microporous crystalline aluminosilicate frameworks, can adsorb hydrogen but are limited by restricted pore volume [7]. Metal hydrides (e.g., MgH_2, $NaAlH_4$) and complex borohydrides (e.g., $LiBH_4$, $NaBH_4$) store hydrogen through chemical bonding, though they generally suffer from slow kinetics and high desorption temperatures [8,9]. More recently, two-dimensional materials such as MXenes, with tunable surface

* Corresponding author.
E-mail addresses: yozdemir@balikesir.edu.tr (Y. Turhan), mdogan@balikesir.edu.tr (M. Doğan), ersinyanmaz@balikesir.edu.tr (E. Yanmaz), zeynepbicil@balikesir.edu.tr (Z. Bicil), bernakocer@balikesir.edu.tr (B.K. Kızılduman).

https://doi.org/10.1016/j.cej.2026.175599
Received 2 January 2026; Received in revised form 21 March 2026; Accepted 25 March 2026
Available online 26 March 2026

chemistries, have emerged as promising candidates for hydrogen storage [10]. Within this broad spectrum, carbon-based materials, including activated carbons [11], carbon spheres [12], carbon nanotubes [13], graphene [14], and fullerenes [15], have attracted particular interest due to their low cost, light weight, high thermal and chemical stability, and ease of functionalization. Their large surface areas and adjustable pore structures make them excellent candidates for hydrogen physisorption, especially under cryogenic conditions. Accordingly, carbon-based materials have become one of the most versatile and scalable platforms for next-generation hydrogen storage technologies [16].

Graphene, a single-atom-thick two-dimensional carbon sheet, has garnered tremendous attention in materials science, chemistry, and biology due to its exceptional electrical conductivity and unique structure. Nevertheless, pristine graphene often lacks sufficient functionality for practical applications, motivating the development of graphene-based hybrids and nanocomposites [17–20]. These composites impart controlled functionality to graphene, thereby enhancing its applicability in energy and environmental fields. Moreover, graphene's outstanding thermal properties improve thermal stability and conductivity in nanocomposites, while its two-dimensional geometry provides a favorable platform for gas adsorption [21]. Fullerenes, on the other hand, are spherical carbon structures with unique electron-accepting properties and high surface reactivity, making them promising candidates for hydrogen storage [22]. Defective fullerenes, in particular, introduce additional binding sites that enhance hydrogen adsorption capacity [15,23]. Lithium doping further optimizes the binding energy of hydrogen molecules by modifying surface electron density, thereby significantly improving storage performance [24,25]. Thus, defect engineering and alkali metal doping are regarded as complementary strategies for enhancing hydrogen storage in fullerene-based systems. Nanocomposites combining graphene and fullerenes have recently drawn attention due to synergistic effects that boost hydrogen storage capacities [26]. However, to the best of our knowledge, this study represents the first systematic experimental evaluation of the hydrogen storage behavior of hybrid nanocomposites comprising defective fullerenes (D—C60) and Li-doped defective fullerenes (Li-D-C60) with graphene. Therefore, we report the hydrothermal synthesis and systematic investigation of graphene-based hybrid nanocomposites incorporating different proportions (1%, 2.5%, and 5%) of defective fullerene (D—C60) and Li-doped defective fullerene (Li-D-C60). The structural, morphological, and surface characteristics of these nanocomposites were comprehensively characterized using Brunauer–Emmett–Teller (BET) analysis, Fourier-transform infrared spectroscopy (FTIR), Raman analysis, Differential thermal analysis/thermogravimetry (DTA/TG), X-ray diffraction (XRD) and Scanning electron microscopy/energy-dispersive X-ray spectroscopy (SEM/EDX). In addition, the amount of lithium incorporated into D—C60 was quantified by atomic absorption spectroscopy (AAS). Furthermore, their hydrogen storage capacities and adsorption kinetics were investigated in detail for the first time. The novelty of this work lies in the simultaneous application of defect engineering and lithium doping in fullerenes, integrated into a graphene matrix to establish a unique hybrid platform for hydrogen storage. Elucidating the synergy between graphene and D-C60/Li-D-C60 is expected to provide valuable insights for the development of next-generation hydrogen storage materials. Finally, this research is aligned with the United Nations Sustainable Development Goals (SDGs). In particular, it contributes to SDG 7 (affordable and clean energy) by promoting renewable and safe energy storage solutions, supports SDG 9 (industry, innovation, and infrastructure) through the development of advanced nanomaterials, and advances SDG 13 (climate action) by fostering the transition toward low-carbon energy systems.

2. Materials and methods

2.1. Materials

Fullerene (C60) and graphene with a purity of 99.9% were procured from Nanografi (Ankara/Türkiye). Lithium, used as the doping agent, was supplied by Sigma-Aldrich. All other reagents and chemicals were of analytical grade and used without further purification.

2.2. Synthesis of hybrid nanocomposites

D—C60 was produced from fullerene by ball milling method [15]. Lithium-doped defective fullerene (Li-D-C60) was synthesized via a hydrothermal approach using $LiNO_3$ as the lithium source. Briefly, 0.5 g of D—C60 was dispersed in 15 mL of 0.1 M $LiNO_3$ solution and transferred into Teflon-lined stainless-steel autoclave (Berghof Reactor Heating System). The suspension was treated at 200 °C under autogenous pressure for 12 h. After natural cooling to room temperature, the obtained solid was filtered, thoroughly washed with deionized water and ethanol to remove residual lithium species, and dried at 105 °C for 24 h [27]. Graphene/D-C60 and graphene/Li-D-C60 hybrid nanocomposites were synthesized using graphene as the matrix and loadings of D—C60 and Li-D-C60 of 1 wt%, 2.5 wt%, and 5 wt%. For each synthesis, the required amounts of graphene and D—C60 (or Li-D-C60), corresponding to 1 g of the final nanocomposite, were separately dispersed in 8 mL of deionized water and subjected to ultrasonication for 30 min to ensure a homogeneous suspension. Then the two suspensions were combined and subjected to ultrasonication for another 30 min. Hydrothermal treatment was conducted in a mechanically stirred Teflon-lined stainless-steel autoclave at 160 °C for 12 h with an internal stirring rate of 300 rpm. After the hydrothermal reaction, the autoclave was allowed to cool naturally to room temperature. The resulting product was filtered, thoroughly washed several times with deionized water to remove residual impurities, and first dried in a conventional oven at 105 °C, followed by vacuum drying at 60 °C for 24 h [28]. All synthesis steps were carried out under identical experimental conditions to ensure the reproducibility and structural consistency of the prepared hybrid nanocomposites.

2.3. Determination of lithium loading in D—C60 by AAS

0.5 g of D—C60 was dispersed in 15 mL of 0.1 M $LiNO_3$ solution and subjected to hydrothermal treatment at 200 °C for 12 h in a Teflon-lined stainless-steel autoclave. After the reaction, the autoclave was naturally cooled to room temperature, and a portion of the supernatant was carefully sampled for lithium analysis. The lithium concentration in the supernatant was determined using a PerkinElmer AAnalyst 200 flame atomic absorption spectrometer (FAAS, Waltham, MA, USA) equipped with a hollow cathode lamp and D_2 background correction. Calibration standards were freshly prepared from a Li stock solution (1000 mg/L, Merck) using ultrapure water within a working range of 0.5–10 mg/L. The difference between the initial Li concentration in the hydrothermal solution (694 ppm) and the measured Li concentration in the supernatant (99.95 ppm) was used to calculate the lithium uptake by the D—C60 sample. Based on this value, the lithium weight percentage and the corresponding Li/C atomic ratio were calculated for the material.

2.4. Characterization

The graphene, graphene/D-C60 and graphene/Li-D-C60 hybrid nanocomposites were comprehensively characterized using FTIR, BET, XRD, Raman, SEM/EDX, and DTA/TG techniques. The functional groups of the hybrid nanocomposites were analyzed using a Perkin Elmer Spectrum 100 FTIR spectrophotometer within the range of 4000–400 cm^{-1}. FTIR spectra were recorded by preparing KBr pellets of the samples. Thermogravimetric (TG) analysis was conducted with a Perkin

Elmer Diamond DTA/TG simultaneous thermal analyzer in the temperature range of 30–1000 °C, under a nitrogen atmosphere at a flow rate of 20 mL/min, with a heating rate of 20 °C/min, to evaluate mass loss behavior of the nanocomposites. The surface morphology and elemental composition were investigated using a Zeiss Evo LS 10 scanning electron microscope equipped with energy-dispersive X-ray spectroscopy (SEM/EDX). Prior to imaging, the samples were sputter-coated with a thin Au/Pd layer for 90 s under a 20 μA current to improve conductivity. Specific surface area and pore structure were determined by Brunauer–Emmett–Teller (BET) analysis using a Quantachrome Nova 2200e instrument (USA). Nitrogen adsorption–desorption isotherms were obtained at 77 K in a volumetric apparatus. Before analysis, the samples were dried at 105 °C for 24 h to remove moisture. Pore size distributions were calculated using the density functional theory (DFT) method for total pore volume, while micropore volume was evaluated using the Dubinin–Radushkevich (DR) method. Crystallographic structures of the nanocomposites were examined by X-ray diffraction (XRD) on a PANalytical Empyrean diffractometer with Cu Kα radiation, operated at 30 mA and 40 kV. Data were collected over a 2θ range of 10°–50° with a scanning rate of 2°/min at room temperature. The Raman spectra of the samples were collected using a WITec alpha 300R micro-Raman system equipped with a 532 nm excitation laser.

2.5. Hydrogen storage

Hydrogen adsorption measurements were carried out using a Hiden IMI-PSI high-pressure volumetric gas sorption analyzer equipped with a cylindrical sample cell. The instrument operates based on the volumetric method, and adsorption capacities are reported as excess adsorption values (mmol/g). No post-measurement conversion to absolute adsorption was performed, thereby avoiding additional uncertainties associated with pore-volume-based corrections. Since a volumetric method was employed, buoyancy corrections applicable to gravimetric systems were not required. Prior to adsorption measurements, 50–100 mg of samples were degassed at 105 °C for 4 h under vacuum until complete pressure stabilization was achieved, ensuring removal of residual adsorbates and verification of system integrity. [15]. The skeletal volume of each sample was determined by helium expansion at room temperature before hydrogen measurements. Dead volume calibration was performed at room temperature, and temperature corrections for cryogenic measurements were automatically applied by the instrument software. The pressure transducers were factory-calibrated, and system stability was verified through pressure monitoring during degassing and prior to gas dosing. Adsorption isotherms were recorded at 298 K and 77 K over the selected pressure range. For cryogenic measurements, the sample cell and connection lines were fully immersed in liquid nitrogen to ensure thermal stability throughout the experiment. The measured sample temperature remained stable at −196.6 ± 0.15 °C (≈77 K) during adsorption. These conditions confirm that true cryogenic thermal equilibrium was maintained during measurements. Equilibrium at each pressure step was defined based on pressure stabilization within predefined dwell times. The equilibration time was set to 5 min below 10 bar and increased progressively up to 15 min near 100 bar, based on preliminary optimization experiments. Representative transient pressure–uptake traces demonstrate rapid stabilization and negligible drift at each pressure step, confirming that equilibrium conditions were achieved within the selected equilibration times. Each isotherm was measured once due to the extended equilibration time required at high pressures. Hydrogen thermodynamic properties were obtained from the integrated NIST REFPROP database, and non-ideal gas behavior under high pressure was accounted for using the Redlich–Kwong–Soave equation of state.

3. Results and discussion

3.1. Characterization

The synthesized hybrid nanocomposites were systematically characterized to determine their structural, morphological, thermal, and surface properties, employing a combination of advanced analytical techniques. These analyses provided comprehensive insights into the physicochemical features of the materials and their suitability for hydrogen storage applications.

3.1.1. FTIR analysis

The FTIR spectra of graphene and, graphene/D-C60 and graphene/Li-D-C60 hybrid nanocomposites are presented in Fig. 1. Pristine graphene exhibits characteristic absorption bands at ~3468 cm^{-1} (–OH group), 2924–2847 cm^{-1} (C—H stretching), and 1374 cm^{-1} (C—H bending), in agreement with its sp^2-hybridized hexagonal lattice structure [29]. The incorporation of D—C60 into graphene leads to the appearance of additional absorption features and shifts in the matrix-related bands, suggesting interactions between the filler and the graphene framework rather than definitively proving strong bonding. For the fullerene phase, reference spectra typically display four prominent bands at 1427, 1182, 576, and 527 cm^{-1}, corresponding respectively to C═C stretching, C—C stretching, and bending modes of the carbon framework [23,29,30]. In the present study, bands in the 1379–1425 cm^{-1} region were clearly observed in the nanocomposites, which is consistent with the presence of D—C60 within the graphene matrix. In Li-doped systems, additional spectral modifications were detected. A broad band in the range of 3431–3466 cm^{-1} may be associated with possible Li—O interactions with oxygen-containing groups on graphene, while shifts in the –OH stretching region suggest potential coordination of Li^+ ions. Moreover, the emergence of bands at 1636–1628 cm^{-1} (C═O stretching), ~1381 cm^{-1} (C—C vibrations coupled with Li), and 1045–1051 cm^{-1} (C—O stretching) indicates possible surface modification upon doping, although definitive assignment would require complementary characterization and peak deconvolution. The progressive increase in the intensity of these characteristic peaks with higher D-C60/Li-D-C60 loading supports the incorporation of fullerene derivatives into the graphene structure. Overall, the observed band shifts and intensity changes in the –OH, C═C, and C—O regions upon Li incorporation suggest that Li ions may act as bridging species between graphene and fullerene domains. These results provide spectroscopic indications of interfacial interactions, consistent with the formation of graphene/D-C60 and graphene/Li-D-C60 hybrid nanocomposites.

3.1.2. Quantification of lithium loading in D—C60

The amount of lithium taken up by the defective fullerene during the hydrothermal process was estimated from the difference between the initial 0.1 M Li concentration (694 ppm) measured by AAS and the Li concentration in the post-processing supernatant (99.95 ppm). According to this calculation, approximately 1.78% of lithium was taken up by the sample, which corresponds to a Li/C atomic ratio of ~0.031. This approach provides a quantitative estimate of the incorporation of lithium into the defect-rich regions of the fullerene skeleton, but the actual incorporation may be slightly lower due to incomplete adsorption or competitive Li loss during the hydrothermal process. This value is significantly lower than the theoretical maximum estimated from the precursor stoichiometry ($Li/C_{60} \approx 2.16$), indicating that only a fraction of the available lithium is incorporated into the defective fullerene structure during the hydrothermal process. The experimentally determined lithium content suggests that Li^+ ions are partially but effectively incorporated into the defect-rich regions of the fullerene framework. Instead of forming a bulk interlayer phase, lithium may have attached to structural defects created during ball milling, where charge transfer from Li to the π-conjugated carbon network can occur. This electron donation induces a local electronic redistribution and enhances defect-

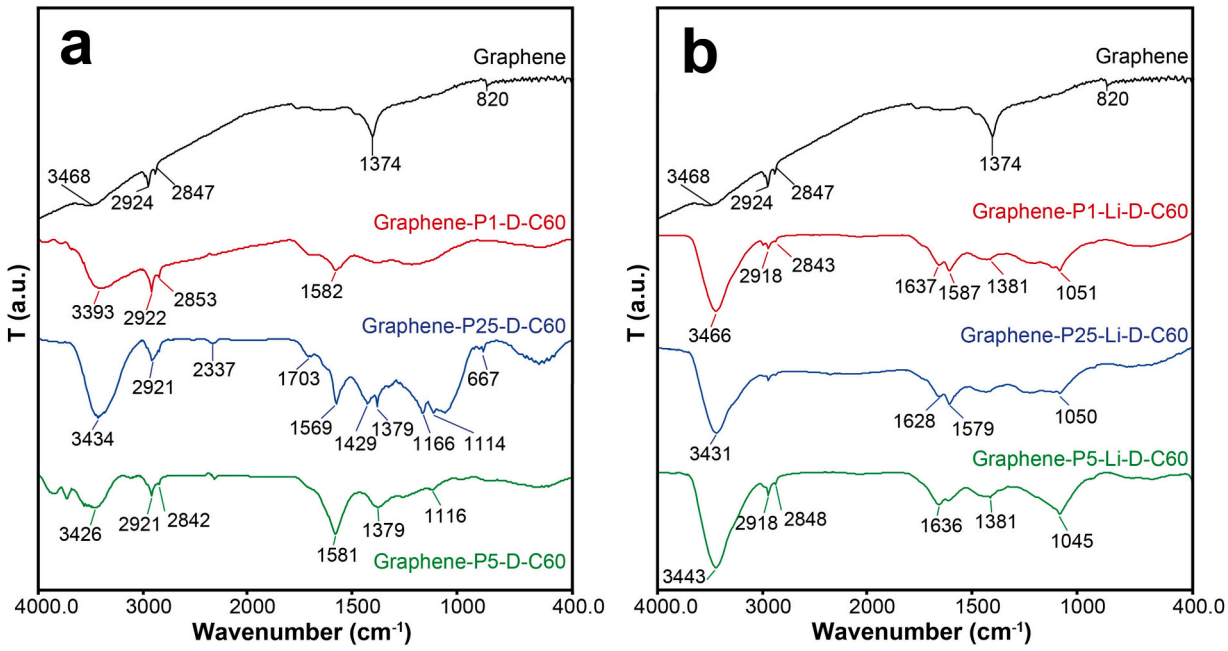

Fig. 1. FTIR spectra of a) graphene and its D—C60 nanocomposites and b) graphene and its Li-D-C60 nanocomposites.

mediated polarization within the carbon lattice. The resulting localized charge imbalance and increased electronic density around defect regions are consistent with the proposed polarization-assisted adsorption mechanism, which is expected to strengthen the interaction between hydrogen molecules and the hybrid carbon skeleton. Additionally, XPS analyses (Li 1s, C 1s, and O 1s) performed in our previous study confirmed the presence of lithium in the D—C60 structure [27], and the AAS results obtained in this work quantitatively support these findings. The Li/C ratio in lithium doping of multi-walled carbon nanotubes and fullerenes is a critical parameter that significantly influences their electronic properties and performance in energy storage applications [31,32]. Li/C ratios in lithium doping vary considerably depending on the carbon structure and experimental doping conditions, ranging from approximately 0.15 to 6:1. The available sources in the literature show significant differences. For fullerenes, Teprovich et al. (2012) obtained a Li:C60 molar ratio of 6:1 under optimized conditions [33], while Deniz et al. (2021) obtained a Li:C = 15:100 (0.15) ratio in computational studies on fullerene-supported graphene [34]. For carbon nanotubes, Yan-Wei et al. (2009) calculated a maximum Li:C ≈ 1:4.75 capacity in double-walled nanotubes [35], and Wen et al. (2010) reported Li:C ≈ 1:2.5 for 4 Å single-walled nanotubes [36]. In contrast, Bendiab et al. (2001) experimentally prepared Li-doped single-walled carbon nanotubes with controlled stoichiometries ranging from 0 to 0.17 (Li:C ≤ 0.17) [37].

3.1.3. Thermal analysis

The thermal degradation behavior of graphene and its D—C60 and Li-doped D—C60 nanocomposites was systematically investigated using TGA, and the TG/[dTG] thermograms are summarized in Fig. S.1 (Supplementary Materials), and the thermal stability parameters obtained from these thermograms are summarized in Table 1. Graphene showed 3 different degradation stages. The first degradation stage started at 41.7 °C with a mass loss of 3.86 wt% at T_{max1} = 66 °C and was attributed to the removal of adsorbed water and moisture on the surface. In the second degradation step, a mass loss of 4.18 wt% occurred at 212 °C. In the third and main degradation step, a mass loss of 17.24 wt% occurred at T_{max3} = 667 °C and left a residue of 72.38 wt% at 1000 °C [38]. The mass loss occurring in the third decomposition step has been attributed in the literature to oxidative pyrolysis of the carbon skeleton

Table 1
Thermal data obtained from TG and d[TG] thermograms of nanocomposites.

Samples	T_{max1} (°C)	ΔY (wt %)	T_{max2} (°C)	$ΔY_2$ (wt %)	T_{max3} (°C)	$ΔY_3$ wt (%)	Residue at 1000 °C (wt %)
Graphene	66	3.86	212	4.18	667	17.24	72.38
Graphene-P1-D-C60	61	1.18	123	2.85	586	12.86	80.06
Graphene-P2.5-D-C60	113	6.25	333	4.23	544	5.20	82.41
Graphene-P5-D-C60	115	6.08	377	3.33	518	6.22	81.44
Graphene-P1-Li-D-C60	67	2.51	368	4.46	603	9.07	81.88
Graphene-P2.5-Li-D-C60	75	3.16	351	3.51	581	6.84	83.83
Graphene-P5-Li-D-C60	65	1.30	404	4.12	539	8.86	83.37

[39]. The approximately 4.18% mass loss observed in the second degradation step has been attributed in the literature to the removal of oxygen functional groups [40,41], which is consistent with the results of the EDX analysis. However, since graphene does not contain oxygen, this usually points to graphene oxide and can be attributed to impurities within the graphene. The incorporation of defective fullerene samples into the graphene matrix led to changes in the temperatures at which the degradation steps occurred. The first degradation step, associated with the removal of surface-adsorbed water and moisture from the structure, shifted to relatively higher temperatures in D-C60-doped nanocomposites compared to graphene (~110 °C). This indicates that the interaction between defective fullerene and graphene restricts the desorption of physically adsorbed species. Similar shifts in initial degradation temperatures have been reported in the literature for polymer-fullerene systems, where interface interactions inhibit volatile matter release and increase carbon residue formation [42]. This increase suggests that the addition of small amounts of fullerene strengthens surface interactions, increases the binding energy of adsorbed moisture,

and delays its release. In fullerene-doped nanocomposites, at the third degradation step corresponding to the main structural degradation of graphene, T_{max3} values decreased significantly from 667 °C to 518 °C depending on the amount of filler. For example, the Graphene-P5-D-C60 nanocomposite showed a T_{max3} value of 518 °C, approximately 149 °C lower than pure graphene. Despite this decrease in T_{max3}, the residue amount at 1000 °C increased to 81.44 wt%, which is approximately 10% higher than that of graphene. This result shows that although fullerene addition destabilizes the degradation temperature by altering the carbon skeleton, it also promotes the formation of more carbonaceous residues. The variability in T_{max3} is consistent with reports that fullerene derivative additives can significantly alter degradation mechanisms and carbon yields depending on their distribution and structural integrity [43]. These results demonstrate that the addition of defective fullerene alters the degradation mechanism of graphene, reducing T_{max3} values but increasing the amount of residue. This dual effect highlights the complex role of fullerene as both a destabilizing agent for thermal initiation and a stabilizing agent for carbon yield during pyrolysis. Thermogravimetric analysis results of nanocomposites obtained by doping Li-D-C60 into a graphene matrix show that lithium doping has a significant improving effect on thermal stability. In all samples containing Li-D-C60, the first mass loss step was observed in the 65–75 °C range, with mass losses varying between 1.30 and 3.16 wt%, indicating a more limited moisture and volatile matter content compared to graphene. In the mid-temperature region, the second degradation step, corresponding to the decomposition of oxygen defects and structurally weak regions, occurred with maximum decomposition temperatures (T_{max2}) in the 351–404 °C range, and mass losses in this step were determined to be at the level of 3.51–4.46 wt%. In the high-temperature region, the third step, corresponding to the degradation of the carbon

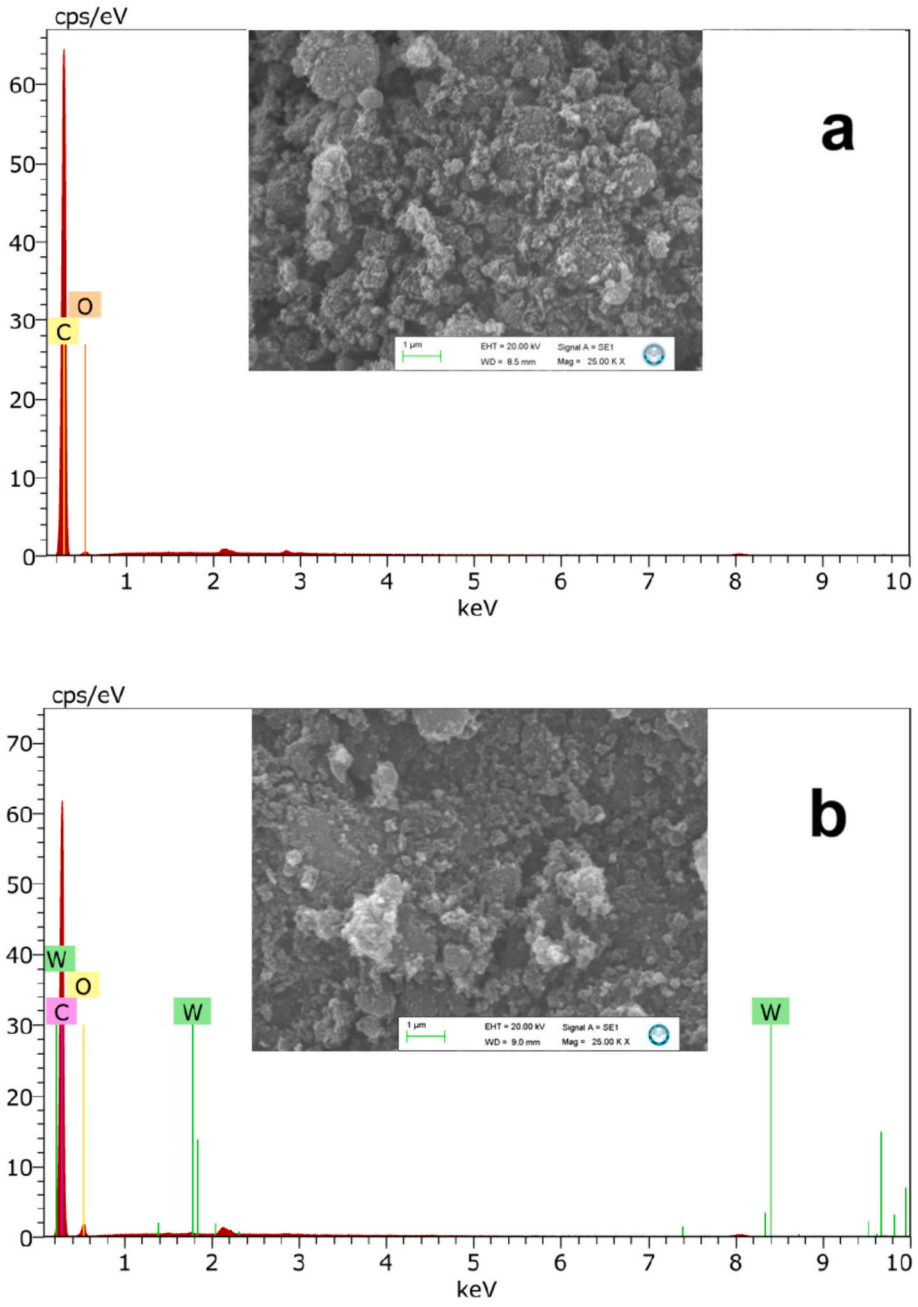

Fig. 2. SEM images and corresponding EDX spectra of (a) Graphene, (b) Graphene-P1-D-C60, (c) Graphene-P2.5-D-C60, (d) Graphene-P5-D-C60, (e) Graphene-P1-Li-D-C60, (f) Graphene-P2.5-Li-D-C60, and (g) Graphene-P5-Li-D-C60.

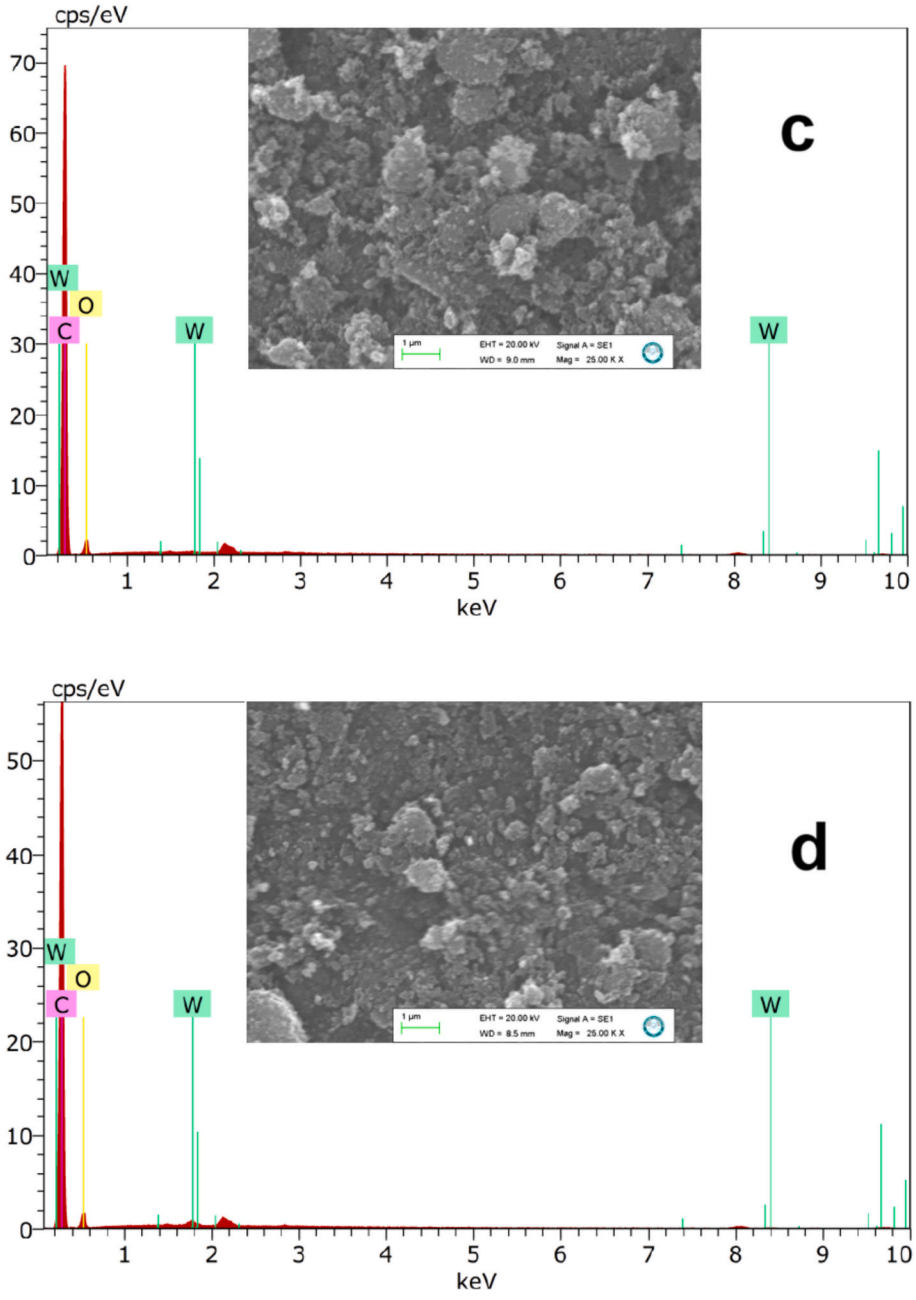

Fig. 2. (*continued*).

skeleton, is characterized by T_{max3} values in the range of 539–603 °C. The relatively low mass losses of 6.84–9.07 wt% occurring at this stage demonstrate that lithium doping increases the thermal resistance of the carbon network. Furthermore, the fact that the residual amounts at 1000 °C are in the range of 81.88–83.83 wt% clearly shows that the Li-D-C60-containing nanocomposites largely maintain their structural integrity even at high temperatures, and that lithium doping plays a role in slowing down thermal degradation in the graphene-fullerene hybrid structure. Li-doped defective fullerene composites not only resist degradation at higher temperatures but also produce more stable carbon structures, consistent with reports in the literature on Li-induced stabilization of carbonaceous nanomaterials [44]. Furthermore, it confirms that Li ions promote cross-linking or bridging effects between graphene and fullerene, thus strengthening the carbon skeleton against oxidative and thermal degradation. A similar behavior has been reported in Li-modified graphene systems, where Li—O coordination strengthens the interfacial bond and delays thermal degradation [45]. Taken together, these findings suggest that defective fullerene doping enhances thermal stability in the graphene matrix over the mid-temperature range, while lithium doping further enhances this effect, reducing volatile losses at low temperatures and significantly limiting the degradation of the carbon skeleton at high temperatures. Specifically, nanocomposites containing Li-D-C60 exhibited the most controlled and robust thermal degradation behavior, with higher T_{max2} and lower ΔY_3 values.

3.1.4. SEM/EDX analysis

The morphological characteristics of graphene-based nanocomposites containing D—C60 and Li-D-C60 were examined by SEM at 25 kX magnification, the morphological findings were further supported by quantifying their elemental compositions with EDX analyses, and the results were given in Fig. 2 and Table 2. The following discussion is based on qualitative evaluation of representative SEM micrographs.

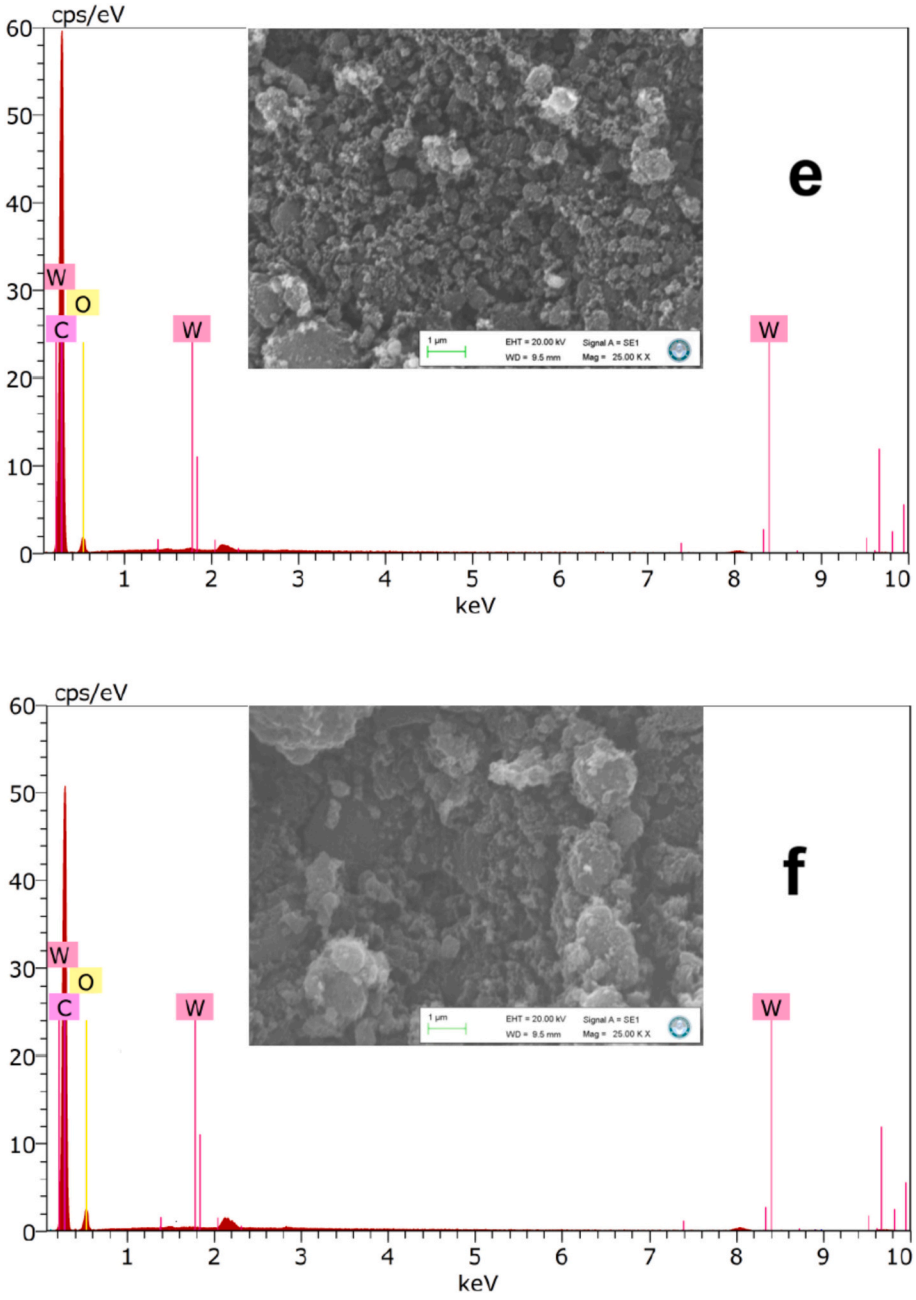

Fig. 2. (*continued*).

Pure graphene exhibited a surface morphology characterized by sheet-like structures with visible stacking and localized agglomeration regions. Compact domains were observed across the surface, consistent with the inherent tendency of graphene layers to restack in the absence of a secondary stabilizing phase. With the incorporation of 1 wt% D—C60, the surface appeared comparatively more dispersed, and large agglomerated domains were less pronounced relative to pristine graphene. Nevertheless, isolated clustered regions remained observable, suggesting that low fullerene loading partially influences surface organization without fully suppressing aggregation. At 2.5 wt% D—C60 loading, the micrographs revealed a more continuous and comparatively uniform surface texture. Fewer visibly compact domains were observed compared to the 1 wt% sample, and the fullerene phase appeared to be distributed across the graphene sheets without forming extensive aggregates. These observations suggest improved dispersion at this composition; however, this interpretation is based on visual assessment rather than statistical image analysis. In contrast, the 5 wt% D—C60 composite displayed the reappearance of localized dense regions and irregular surface features. The increased filler content appeared to promote partial re-aggregation, resulting in a less uniform morphology compared to intermediate loading. A similar trend was observed in Li-doped systems. The 1 wt% Li-D-C60 nanocomposite exhibited relatively fine surface features distributed over the graphene sheets. At 2.5 wt% loading, regions containing comparatively larger clusters became visible, and the distribution appeared less uniform than at lower loading. When the Li-D-C60 content was increased to 5 wt%, more pronounced aggregation zones and overlapping particulate domains were observed, indicating that higher dopant concentrations may contribute to surface heterogeneity. Overall, SEM observations indicate a loading-dependent influence of defective and Li-doped fullerenes on graphene morphology. Nevertheless, further quantitative image analysis would be required to establish statistical significance.

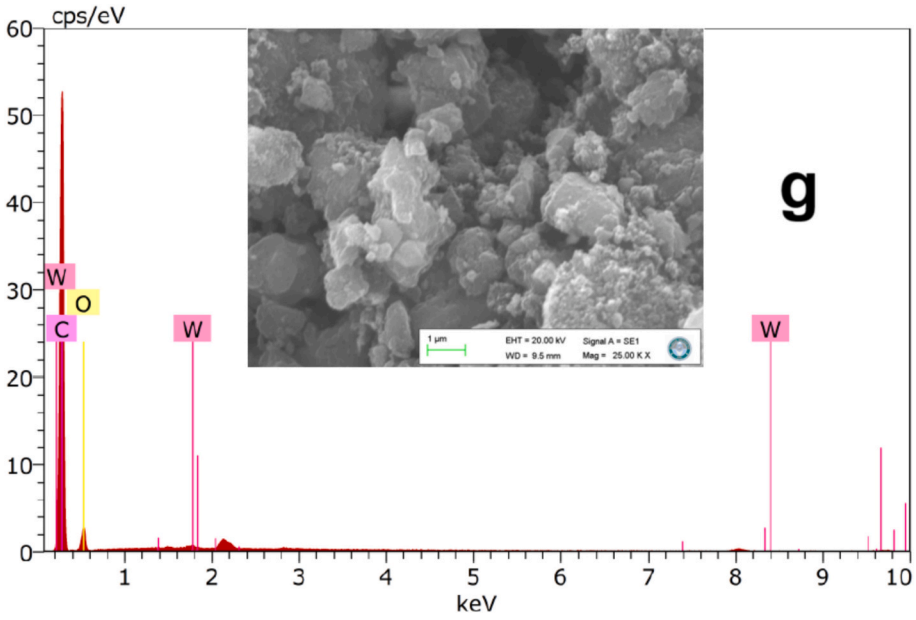

Fig. 2. (*continued*).

Table 2
% elemental composition of graphene and its nanocomposites.

Samples	C (wt%)	O (wt%)	W (wt%)	Other elements (wt%)
Graphene	95.77	4.23	–	–
Graphene-P1-D-C60	87.68	9.81	0.64	1.87
Graphene-P2.5-D-C60	87.19	10.41	0.70	1.70
Graphene-P5-D-C60	86.98	9.98	1.51	1.53
Graphene-P1-Li-D-C60	87.61	10.22	0.58	1.59
Graphene-P2.5-Li-D-C60	82.80	13.87	1.08	2.25
Graphene-P5-Li-D-C60	82.78	14.08	1.27	1.87

In EDX spectra in Fig. 2, graphene contained 95.77% carbon and 4.23% oxygen, reflecting minimal oxygenated functional groups. With the addition of D—C60, the carbon content gradually decreased to 87.68% (1 wt%), 87.19% (2.5 wt%), and 86.98% (5 wt%). Simultaneously, oxygen levels increased, reaching a maximum of 10.41% at 2.5% loading. This increase in oxygen content is consistent with the presence of oxygenated groups arising from the ball milling process used to produce defective fullerene [15]. At 5 wt%, the oxygen content in D—C60 decreased slightly to 9.98%; this could be attributed to the fullerene not being fully dispersed within the matrix or to signal suppression by the carbon-enriched graphene phase. The maximum oxygen enrichment observed at 2.5 wt% confirms that this composition exhibits the highest oxygen functional group density on the surface, which is further correlated with the optimum morphology seen in the SEM images. Li doping intensified these compositional changes. In the Li-D-C60 series, while carbon content decreased from 87.61% at 1 wt% to 82.78% at 5 wt%, oxygen levels increased from 10.22% to 14.08%. The 2.5 wt% Li-D-C60 nanocomposite showed the highest oxygen content (13.87%), indicating enhanced surface oxidation and functionalization facilitated by lithium. These results demonstrate that Li ions alter the surface chemistry by promoting the incorporation of oxygenated groups. In all samples, trace amounts of W, Al, and Cu were detected in the spectra, which are most likely associated with sample preparation or environmental contamination rather than intrinsic components of the nanocomposites [15]. For example, tungsten is related to the milling process, while Al and Cu are attributed to sample carrier artifacts. Overall, the SEM and EDX analyses clearly demonstrate that both the morphology and surface chemistry of the nanocomposites are strongly dependent on the type and loading of the filler. The results confirm that defective fullerene incorporation improves dispersion at moderate loadings, while Li doping enhances oxygen functionalization and interfacial interactions. However, excessive filler ratios (>2.5 wt%) promote agglomeration and reduce structural homogeneity, emphasizing the importance of optimizing loading ratios to achieve stable and uniform nanocomposite architectures.

3.1.5. XRD analysis

Fig. 3 presents the XRD patterns of graphene and D—C60 and Li-D-C60 doped nanocomposites. Reflections were observed in the graphene XRD pattern at angles $2\theta = 22.63^\circ$, 26.77°, 28.43°, 42.65°, and 44.53°. The dominant peak at $2\theta = 26.77^\circ$ corresponds to the graphitic (002) plane and represents the stacking of sp^2 hybridized carbon layers. The d-spacing value calculated from this peak is approximately 3.329 Å, indicating that a certain long-range order is maintained between the graphene layers (Table S.1 in Supplementery Mateials). Furthermore, the narrow FWHM value of the peak (0.0631°) reveals the presence of a relatively orderly graphitic stacking in the structure. These findings are consistent with graphene and graphitic carbon structures reported in the literature [38,40,46,47]. The weak reflection observed at $2\theta = 22.63^\circ$ suggests that the interlayer distance is widened in places and that partial exfoliation may have occurred in the structure. The low-intensity peak around $2\theta \approx 28.43^\circ$ can be associated with the turbostratic stacking reported in graphene structures. The reflections observed at high angles, $2\theta = 42.65^\circ$ and 44.53°, are attributed to planes (100) and (101), respectively, supporting the idea that the three-dimensional long-range crystalline order is limited and the two-dimensional graphene-like structure is dominant [38,40,46,47]. Quantitative changes in the position and width of the graphitic (002) peak were observed in D-C60-doped nanocomposites, and the numerical values are given in Table S.1. In the P1-D-C60 sample, it was determined that the (002) peak shifted to $2\theta \approx 26.61^\circ$ and the d-spacing value increased to 3.350 Å. This indicates an increase in the distance between the graphene layers. The significant increase in the FWHM value (0.5047°) in the same sample reveals a decrease in the interlayer correlation length and a weakening of the crystal order. In the P2.5-D-C60 and P5-D-C60 samples, the shift of the (002) peak to higher angles and the decrease in the d-spacing value suggest that a limited rearrangement may occur depending on the doping ratio. However, the fact that the FWHM values are higher in all D-C60-doped samples compared to graphene indicates that long-range

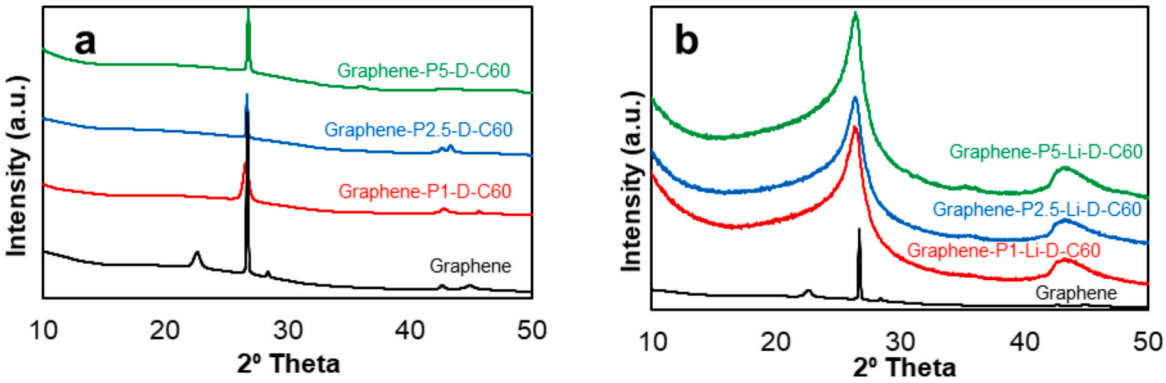

Fig. 3. XRD patterns of a) graphene and its D—C60 nanocomposites and b) graphene and its Li-D-C60 nanocomposites.

graphitic stacking is not fully preserved and a more disordered carbon structure is formed. More pronounced structural changes were observed in nanocomposites containing Li-D-C60 (Table S.1). In the P1-Li-D-C60 sample, d-spacing was determined as 3.346 Å ($\Delta d \approx 0.50\%$), while in the P2.5-Li-D-C60 sample, this value increased to 3.359 Å and the highest expansion rate ($\Delta d \approx 0.88\%$) was obtained. In the P5-Li-D-C60 sample, d-spacing was calculated as 3.340 Å ($\Delta d \approx 0.33\%$). These results show that the presence of Li is more effective in increasing the distance between graphene layers. The wider and lower intensity of the (002) peak in Li-doped systems reveals a decrease in the interlayer correlation length and a greater disruption of the graphitic order. This trend suggests that lithium weakens the stacking order by modifying the interaction between the carbon layers. The broad amorphous-like signal observed, particularly in the P5-Li-D-C60 sample, indicates that the structure is largely disordered and transformed into a hybrid carbon network with high defect density. The absence of sharp peaks specific to Li in the XRD patterns suggests that lithium does not form a separate crystalline phase and may be distributed homogeneously in small amounts within the structure. Similarly, the absence of prominent reflections characteristic of fullerene crystals indicates that the D—C60 phase is well dispersed within the graphene matrix and forms a hybrid carbon structure rather than a separate crystalline phase. Although XRD analysis does not directly elucidate the intercalation mechanism, it provides quantitative indicators of structural evolution based on peak position, d-spacing and FWHM changes (Fig. 3 and Table S.1). In conclusion, while D—C60 doping leads to limited interlayer distance changes and partial crystallinity reduction in the graphene matrix, Li-D-C60 doping makes this effect more pronounced and modifies the graphitic stacking order more strongly. The systematic 2θ shifts and d-spacing changes in peak (002) provide quantitative evidence of doping type-dependent structural evolution and are consistent with trends reported in the literature for alkali metal-doped carbon systems [38,40,46,47].

3.2. Hydrogen storage

In this section, the hydrogen storage behaviors of graphene and its nanocomposites synthesized via the hydrothermal method are discussed by jointly evaluating the combined effects of BET surface area, pore volume, temperature, deffective sites, doping, pressure conditions, and filler loading. A detailed examination of the interrelationships among these parameters will meaningfully contribute to a better understanding of the adsorption mechanisms of the materials. Fig. 4 presents the pressure-dependent hydrogen storage capacities of graphene and its D—C60 and Li-D-C60 hybrid nanocomposites at room and cryogenic temperatures. The literature indicates that the hydrogen storage capacities of solid adsorbents are closely related to BET surface area and/or pore volume [15,48]. The nitrogen adsorption–desorption isotherms of the same samples, where all exhibit typical Type IV isotherms, are indicative of a pronounced mesoporous character (Fig. S.2 in Supplementary Materials). The sharp uptake at low relative pressures ($p/p_0 < 0.1$) corresponds to micropore filling. The width of the hysteresis loop appearing in the high-pressure region is particularly proportional to the mesopore volume [49]. BET surface areas calculated from these isotherms are summarized in Table 3. In addition, the cumulative pore volume–pore width relationships for the same samples are given in Fig. 5, and the micro-, meso-, and macropore volumes calculated by the DFT method are also listed in Table 3.

When the hydrogen adsorption isotherms for all samples at room-temperature in Fig. 4 are examined, the storage capacity increases linearly with pressure. This behavior can be explained by Henry's law: at low to moderate pressures, the amount of gas adsorbed is directly proportional to pressure. As pressure rises, the density of hydrogen gas in the system increases and more H_2 molecules per unit volume contact the surface. The active sites on the surface fill rapidly; with increasing pressure, new molecules adsorb onto less accessible regions. The principal reason that hydrogen adsorption capacities obtained at cryogenic temperatures (−196 °C) are markedly higher than those at room temperature is that van der Waals interactions become dominant at low temperatures. At room temperature, hydrogen molecules possess high kinetic energy, so they bind only transiently to surface active sites and readily desorb. In contrast, at low temperature the kinetic energy of the molecules decreases significantly; their interactions with the surface become more stable, and reversible physisorption occurs more strongly. At 77 K, hydrogen exists in a supercritical state, and its adsorption behavior is governed by supercritical fluid–solid interactions rather than classical phase-transition mechanisms. Under these conditions, deviations from ideal Langmuir behavior at intermediate pressures (around 50 bar) reflect progressive pore filling and fluid densification within the confined micro- and mesoporous structure. The observed increase in uptake arises from enhanced excess adsorption associated with density amplification inside the pores. Consequently, at cryogenic temperatures the pressure-dependent increase in capacity stems not only from the rise in bulk gas density but also from confinement-induced density enhancement within the porous network. Therefore, hydrogen storage isotherms exhibit a steeper increase at low temperatures, and the total capacity becomes considerably higher than at room temperature.

Graphene has a high BET surface area of 744 m^2/g and a total pore volume of 0.929 cm^3/g, providing a strong starting point for hydrogen storage capacity. In particular, a micropore volume of 0.310 cm^3/g together with a mesopore volume of 0.527 cm^3/g shows that graphene features both micropores that afford high surface area and mesopores that facilitate gas diffusion. These characteristics are critical for hydrogen binding to the surface and diffusion into the pores. According to the results in Fig. 4a, pristine graphene reaches a hydrogen storage capacity of 0.89 wt% at room temperature, rising to 1.81 wt% at cryogenic temperature. The roughly two-fold increase under cryogenic conditions is attributed to stronger van der Waals interactions and more

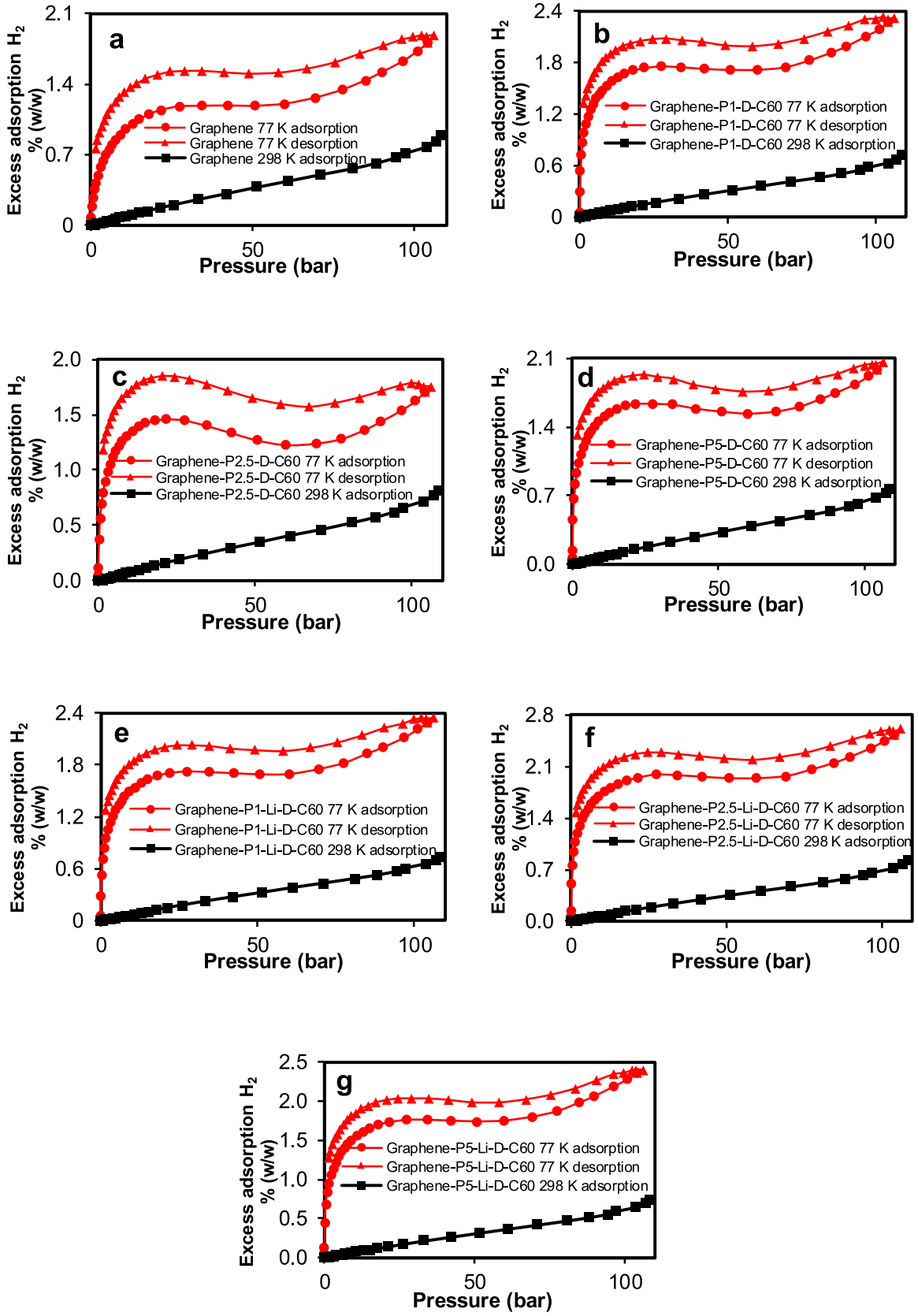

Fig. 4. Hydrogen storage capacities of a) graphene, b) Graphene-P1-D-C60, c) Graphene-P2.5-D-C60, d) Graphene-P5-D-C60, e) Graphene-P1-Li-D-C60, f) Graphene-P2.5-Li-D-C60 and g) Graphene-P5-Li-D-C60 at room and cryogenic temperatures.

Table 3
BET surface area and pore volume data of graphene and its nanocomposites.

Samples	S_{BET} (m^2/g)	V_t (cm^3/g)	V_{micro} (cm^3/g)	V_{DFT} (cm^3/g)	V_{meso} (cm^3/g)	V_{macro} (cm^3/g)
Graphene	744	0.929	0.310	0.837	0.527	0.092
D-C60	169	0.1723	0.072	0.1509	0.079	0.0214
Graphene-P1-D-C60	720	0.732	0.301	0.663	0.362	0.069
Graphene-P2.5-D-C60	693	0.711	0.291	0.641	0.350	0.070
Graphene-P5-D-C60	707	0.741	0.295	0.669	0.374	0.072
Li-D-C60	219	0.168	0.091	0.148	0.057	0.020
Graphene-P1-Li-D-C60	732	0.934	0.305	0.833	0.528	0.101
Graphene-P2.5-Li-D-C60	741	0.920	0.308	0.825	0.517	0.095
Graphene-P5-Li-D-C60	725	0.982	0.305	0.874	0.569	0.108

effective utilization of the pore network at low temperature.

Fig. 4b–d shows the hydrogen storage capacities of the graphene/D-C60 hybrid nanocomposites at room and cryogenic temperatures. While the capacities of the hybrid nanocomposites decrease slightly at room temperature, they increase markedly at cryogenic temperature. In our previous work, when defective fullerene was produced from fullerene, the hydrogen storage capacity at room temperature increased slightly from 0.80 wt% to 0.82 wt%, whereas at cryogenic temperature it rose from 1.90 wt% to 2.17 wt% [15]. Thus, D—C60 exhibited a 2.65-fold increase in storage capacity at cryogenic temperature relative to room temperature. The changes measured in BET surface area and pore properties upon loading D—C60 into the graphene matrix (1, 2.5, and 5 wt%) should be interpreted as the net result of two opposing effects: (i) partial restacking and pore-mouth blocking arising from π–π interactions between D—C60 and graphene layers; and (ii) the behavior of D—C60 spheres as "spacers," which partially suppress complete restacking between layers and preserve mesopore accessibility. The fact that the N_2 isotherms display Type IV character with hysteresis for all samples confirms that the mesoporous framework is retained (Fig. S.2 in Supplementary Materials). A similar trend is observed for hydrogen adsorption among graphene and its nanocomposite samples (Fig. 4b–d). Table 3 quantitatively supports this balance. For Graphene-P1-D-C60, S_{BET} = 720 m^2/g, V_{micro} = 0.301 cm^3/g, and V_{meso} = 0.362 cm^3/g; for Graphene-P2.5-D-C60, S_{BET} = 693 m^2/g, V_{micro} = 0.291 cm^3/g, and V_{meso} = 0.350 cm^3/g; and for Graphene-P5-D-C60, S_{BET} = 707 m^2/g, V_{micro} = 0.295 cm^3/g, and V_{meso} = 0.374 cm^3/g. In the same table, graphene shows S_{BET} = 744 m^2/g, V_{micro} = 0.310 cm^3/g, and V_{meso} = 0.527 cm^3/g, while D—C60 shows S_{BET} = 169 m^2/g, V_{micro} = 0.072 cm^3/g, and V_{meso} = 0.079 cm^3/g. Thus, relative to graphene, the nanocomposite hybrids exhibit a slight decrease in surface area/mesopore fraction, whereas compared to D—C60 they show a pronounced increase. The changes observed in surface area and pore volumes of the graphene/D-C60 hybrid nanocomposites directly affect hydrogen storage capacity. Owing to this pore structure, hydrogen storage isotherms are governed by different parameters at two temperatures. At room temperature, Henry's law is dominant; thus, the adsorbed amount largely scales with accessible surface area and open mesopores. The slight decrease in S_{BET}/V_{meso} observed in the hybrids relative to graphene corresponds to a reduction in room-temperature capacity (Graphene > Graphene-P2.5-D-C60 > Graphene-P5-D-C60 > Graphene-P1-D-C60; D—C60 remains limited due to its low S_{BET}). This explanation aligns well with the methodological principles of the IUPAC standard for physisorption isotherm classification and data presentation [49].

At 77 K, capacity is governed not only by S_{BET} but also by the micro/ultra-micropore size and the layer–gas interaction energy. The widely accepted Chahine correlation at 77 K (approximately ~1 wt% H_2 per ~500 m^2/g) has been observed across a broad range of materials, although with optimal microporosity and/or defect-induced interactions

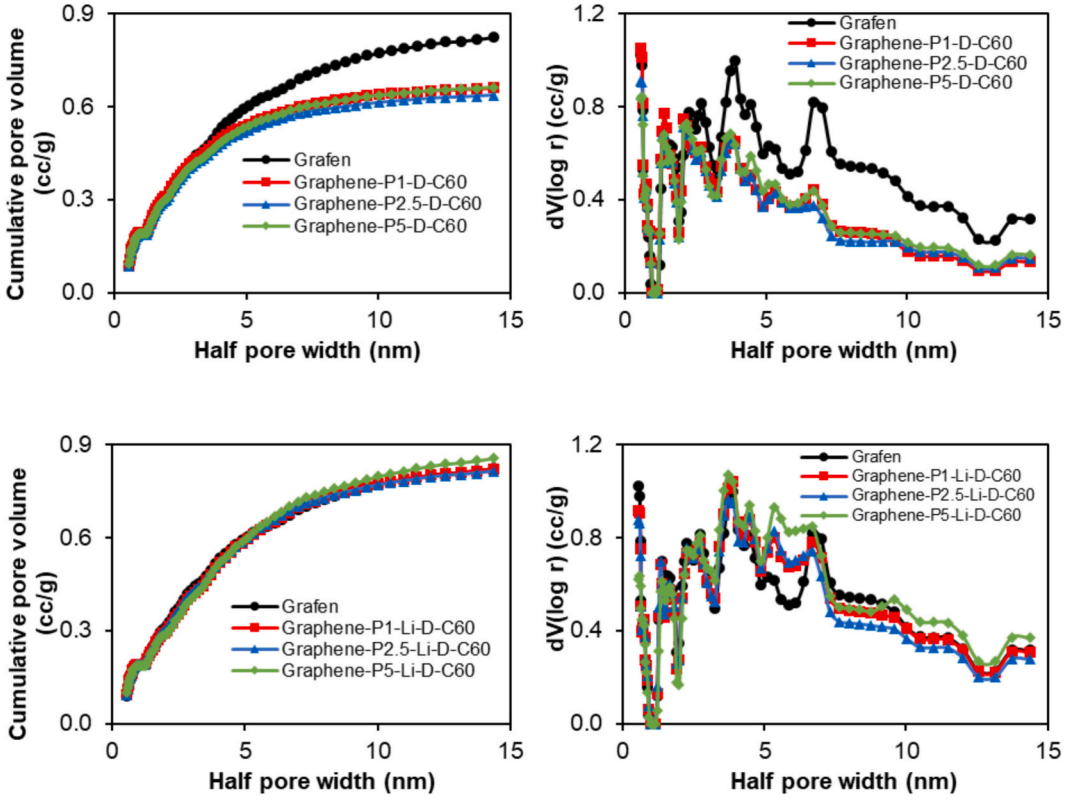

Fig. 5. Change of cumulative pore volumes of graphene and its nanocomposites with half pore width.

this line can be locally exceeded [6]. In the hybrid nanocomposites, V_{micro} values are very close to that of graphene (0.301, 0.291, and 0.295 cm^3/g), and the presence of mesoporosity in all samples (Type IV + hysteresis) helps rationalize the capacity increases/decreases observed at 77 K. Graphene-P1-D-C60 nanocomposite has a surface area of 720 m^2/g and a total pore volume of 0.732 cm^3/g, both lower than those of graphene (Table 3). Although the micropore volume is preserved at 0.301 cm^3/g, the mesopore volume decreases to 0.362 cm^3/g. The reduction in mesoporosity shortens diffusion pathways and partially blocks access to adsorption sites. Despite the decreases in BET surface area and mesopore volume, hydrogen storage capacity increases noticeably at cryogenic temperature. While graphene has a storage capacity of ~1.81 wt% around 100 bar at cryogenic temperature, the Graphene-P1-D-C60 hybrid reaches ~2.30 wt%. This corresponds to an improvement of ~27 wt%. The Graphene-P1-D-C60 hybrid best balances the "spacer ↔ blocking" trade-off, preserving micro-scale accessibility. This structural balance is further supported by Raman spectroscopy (Fig. 6a), where the I_D/I_G ratio decreases from 0.972 for graphene to 0.942 for Graphene-P1-D-C60 nanocomposite, indicating a slight reduction in structural disorder. The decrease in I_D/I_G suggests that π–π interactions between graphene layers and D—C60 may partially stabilize the sp^2 carbon network, thereby maintaining electronic continuity while preserving accessible adsorption regions.

When D—C60 loading is raised to 2.5 wt%, the surface area falls to 693 m^2/g and the total pore volume to 0.711 cm^3/g (Table 3). The micropore volume is 0.291 cm^3/g and the mesopore volume 0.350 cm^3/g. In Fig. 5, a distinct narrowing is observed in the cumulative pore-volume curve of this sample, with a reduction in pore size particularly in the 2–10 nm range. This narrowing restricts hydrogen diffusion and adversely affects capacity. Accordingly, the hydrogen capacity remains below that of graphene at room temperature and is measured as 1.71 wt % under cryogenic conditions (Fig. 4c), about 5% lower than graphene. Here, capacity loss can be attributed to the decrease in surface area and pore volume as well as partial blockage of pore channels by D—C60 particles. Consistently, Raman spectra (Fig. 6a) show an increase in the I_D/I_G ratio to 0.958 for Graphene-P2.5-D-C60, reflecting enhanced structural disorder and interfacial heterogeneity. This rise in defect density indicates that fullerene-induced lattice perturbations begin to outweigh the stabilizing spacer effect, leading to partial disruption of pore continuity and reduced adsorption efficiency. In Graphene-P2.5-D-C60, blocking/dilution effects become pronounced and capacity decreases.

The 5 wt% D-C60-loaded nanocomposite shows a surface area of 707 m^2/g and a total pore volume of 0.741 cm^3/g (Table 3). The micropore volume is 0.295 cm^3/g and the mesopore volume 0.374 cm^3/g. These values are slightly higher than those of Graphene-P2.5-D-C60, indicating a partial increase in pore volume. Although its hydrogen storage capacity remains below that of graphene at room temperature, it is recorded as 1.99 wt% under cryogenic conditions (Fig. 4d). Partial improvement in V_{meso} in Graphene-P5-D-C60 increases diffusion and partially increases capacity, but does not reach the optimum due to pore size reduction and gravimetric dilution. The Raman data (Fig. 6a) further confirm this trend, with the I_D/I_G ratio increasing to 0.962 for Graphene-P5-D-C60, demonstrating progressive defect generation at higher fullerene loading. Although defect sites can enhance local adsorption potentials, excessive disorder may weaken long-range graphitic coherence and partially compromise pore accessibility, preventing attainment of the optimal capacity observed at lower loading. This behavior is consistent with experimental/theoretical studies showing that at 77 K H_2 adsorption is modulated by pore size and interaction energy. For example, Deniz et al. (2021) showed that inserting undoped fullerene units between graphene layers increases the physical adsorption capacity of hydrogen relative to graphene alone, chiefly for structural reasons. Fullerenes activate both their own inner/outer surfaces and the opposing faces of graphene layers, thereby increasing accessible surface area and accessible pore volume and providing a greater number of more favorable binding regions for van der Waals-driven physisorption. This structure preserves the high-potential fields afforded by micropores (especially in the ultra-micro region) while delivering a multimodal pore-size distribution that enhances diffusion accessibility through the mesopore contribution. As a result, capacity at low pressure and cryogenic temperature is largely determined by gravimetric surface area, whereas at higher pressures accessible pore volume and the additional access pathways provided by the mesopore component become more prominent. The Type I character of the isotherms and the "total ≈ excess" convergence at low pressure are also consistent with the purely physisorptive nature of the system. In this framework, adding undoped fullerene to the graphene matrix increases H_2 capacity significantly via structural/geometric optimization without requiring chemical bonding [50].

In conclusion, D—C60 loading modulates the hydrogen storage performance of graphene in a loading-sensitive manner. In Graphene-P1-D-C60 sample, a higher capacity than graphene is obtained; this can be attributed to D—C60 acting as a spacer, limiting interlayer restacking, preserving micro/ultra-micro pore accessibility, and not blocking mesopore diffusion pathways. Raman analysis (Fig. 6a) corroborates this interpretation by demonstrating moderated defect density at low loading. In Graphene-P2.5-D-C60, capacity falls below that of graphene; here, pore-blocking and gravimetric dilution become dominant, limiting accessible adsorption sites and pore entrances. The concurrent increase in I_D/I_G confirms intensified structural perturbation. In Graphene-P5-D-C60, the capacity surpasses that of graphene but remains below that of Graphene-P1-D-C60; while the increase in V_{meso} partially improves diffusion, pore narrowing and partial restacking prevent attainment of the optimum. The higher I_D/I_G value observed in Raman spectra indicates excessive defect formation at this composition.

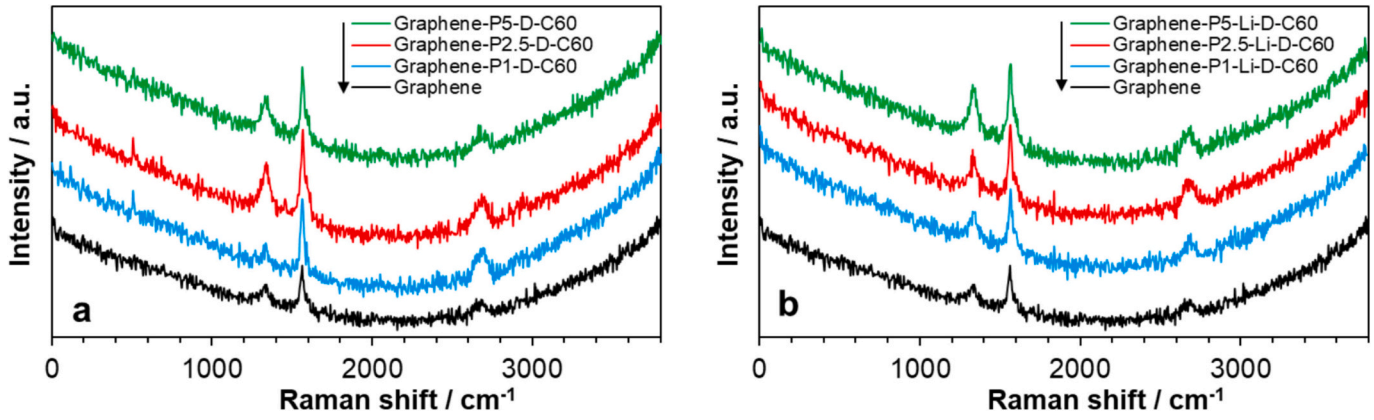

Fig. 6. Raman spectra of (a) graphene and graphene–D-C60, and (b) graphene and graphene–Li-D-C60 hybrid nanocomposites.

This outcome shows that capacity depends not only on total surface area but also on the balance between accessible micropores, mesopore continuity, and controlled defect density. The combined textural (BET/pore volume) and spectroscopic analyses clearly demonstrate that an optimum structural state, characterized by moderated disorder and preserved pore accessibility, governs the superior cryogenic hydrogen storage behavior. From an application standpoint, low D—C60 loadings (where the spacer effect dominates and disorder is minimized) are advantageous for achieving high capacity under cryogenic conditions, whereas at moderate and higher loadings, pore-blocking-induced losses in accessibility and excessive defect formation limit performance.

Fig. 4e–g and Table 3 show that Li-doped defective fullerenes (Li-D-C60) enhance the hydrogen storage performance of graphene, particularly under cryogenic conditions. In Graphene-P1-Li-D-C60, $S_{BET} = 732$ m^2/g and $V_t = 0.934$ cm^3/g are very close to the parameters of graphene ($S_{BET} = 744$ m^2/g, $V_t = 0.929$ cm^3/g); the individual pore volumes $V_{micro} = 0.305$, $V_{meso} = 0.528$, and $V_{macro} = 0.101$ cm^3/g are likewise nearly identical. This suggests that P1-Li-D-C60 does not disrupt the pore structure; on the contrary, it slightly increases the total pore volume (from 0.929 to 0.934 cm^3/g). Raman spectra (Fig. 6b) further support this structural preservation: the I_D/I_G ratio of Graphene-P1-Li-D-C60 (0.970) is very close to that of graphene (0.972), indicating that Li incorporation at low loading does not significantly increase lattice disorder and that the sp^2 carbon framework remains largely intact.

The Graphene-P1-D-C60 sample exhibits a storage capacity of 0.744 wt%, which is lower than that of graphene (0.89 wt%); however, at 77 K the capacity rises to 2.30 wt%, surpassing the 1.81 wt% of graphene. This increase indicates that at low temperature Li-induced surface charging/polarization adds to the van der Waals interactions with H_2 and creates new/local binding sites [25]. The near-constant I_D/I_G ratio observed in Fig. 6b suggests that this enhancement is not driven by excessive structural disorder but rather by Li-induced electronic modulation on a structurally preserved graphene framework.

In Graphene-P2.5-Li-D-C60, $S_{BET} = 741$ m^2/g and $V_t = 0.920$ cm^3/g indicate that the pore structure is largely preserved ($V_{micro} = 0.308$, $V_{meso} = 0.517$, $V_{macro} = 0.095$ cm^3/g). Fig. 4f shows that the capacity remains below that of graphene at room temperature (0.82 wt%) but rises to 2.53 wt% at 77 K, clearly exceeding the 1.81 wt% capacity of graphene. The homogeneous mesopore distribution in the 2–10 nm range and the preserved micropore component seen in Fig. 5 suggest that optimization of the diffusion–storage balance is near-optimal in this sample. Raman analysis reveals a slight decrease in the I_D/I_G ratio to 0.967, indicating moderated structural reorganization and a controlled level of Li-induced defect formation. This balanced defect density likely contributes to enhanced local polarization without significantly compromising graphitic coherence or pore continuity. This observation is consistent with the literature, which emphasizes that at 77 K capacity is determined not only by S_{BET} but also by micro/ultra-micropore size and interaction energy [49,51,52].

Although $S_{BET} = 725$ m^2/g in Graphene-P5-Li-D-C60, the highest total pore volume in the series is recorded with $V_t = 0.982$ cm^3/g ($V_{micro} = 0.305$, $V_{meso} = 0.569$, $V_{macro} = 0.108$ cm^3/g). Fig. 4g shows that the hydrogen storage capacity remains low at room temperature; however, at 77 K it reaches 2.36 wt%, slightly lower than that of the Graphene-P2.5-Li-C60 sample but still higher than graphene. While the marked increase in mesopore volume facilitates diffusion, the high Li loading can limit the accessible micro-fraction through partial pore-blocking, geometric constriction, and possible Li clustering, leading to sub-optimal capacity. Consistently, Raman spectra (Fig. 6b) show an increase in I_D/I_G to 0.973 for Graphene-P5-Li-D-C60, indicating enhanced structural disorder at higher Li loading. This increase suggests that excessive Li incorporation induces additional $sp^2 \rightarrow sp^3$ hybridization and local lattice distortion, which may partially reduce electronic continuity and accessible micropore fraction despite the larger total pore volume.

This optimal-loading behavior agrees with computational predictions that in Li-doped fullerene/graphene systems, increasing the doping dose initially boosts capacity but subsequently limits accessibility [50]. The above results confirm that the triad of defect chemistry, doping density, and hybrid architecture jointly governs cryogenic H_2 storage. The Raman-derived I_D/I_G evolution across the series (0.970 → 0.967 → 0.973) clearly demonstrates that hydrogen storage enhancement correlates with a controlled, non-monotonic modulation of structural disorder rather than a simple increase in defect density.

The 2.17 wt% capacity of single-phase D—C60 is higher than that of pristine C60, because vacancies, ring transformations (Stone–Wales), and edge defects enhance H_2 storage in micropore dimensions and increase the local adsorption potential [51,52]. Direct Li doping of the same material lowers capacity to 1.90 wt%, because Li atoms on defective surfaces induce local $sp^2 \rightarrow sp^3$ hybridization and partial pore-blocking, narrowing accessible pore sizes and reducing the diversity of active sites. This finding is consistent with studies reporting that the favorable electronic effect of Li (charge transfer/polarization), which increases binding energy, may not translate into a net gain, particularly when geometric constraints are present [25].

In the graphene nanocomposites of Li-D-C60, graphene's high BET surface area and mesoporous structure provide new diffusion pathways, while Li-D-C60 units act as spacers between layers, limiting restacking and preserving micropore accessibility. At low–moderate Li loadings, the electronic enhancement imparted by Li (charge transfer that polarizes H_2) is co-optimized with geometric accessibility; this is embodied in the 2.53 wt% peak capacity observed for Graphene-P2.5-Li-D-C60. At higher loading (Li-P5-D-C60), even though the total pore volume increases, the fraction of accessible micropores and the entry apertures within defective fullerene structures become partially restricted, leading to a decrease in hydrogen storage capacity to 2.36 wt%.

Overall, the combined textural (BET/pore structure) and spectroscopic evidence indicates that optimum cryogenic hydrogen storage is achieved when Li-induced electronic polarization is balanced with controlled structural disorder, preserving graphitic coherence and micropore accessibility. This integrated mechanism shows that, at 77 K, the hydrogen storage capacity depends not only on surface area but also on pore size and interaction energy, and that the hybrid design combined with controlled Li doping yields a more stable and sustainable performance improvement than single-phase doping [49–52].

Within this framework, the best cryogenic performance in graphene/Li-doped defective fullerene hybrids is achieved when (i) the pore structure is preserved without degradation, (ii) accessibility in the micro/ultra-micro range is maintained together with a homogeneous mesoporous network, and (iii) the Li loading does not disrupt the balance between "electronic enhancement + geometric accessibility." This balance is experimentally supported by the combined BET, pore-size distribution, and Raman I_D/I_G evolution, which indicate controlled defect modulation without excessive structural distortion. Therefore, the 2–3 wt% loading ratio emerges as a rational target range. In particular, the non-monotonic variation of structural disorder (I_D/I_G) across the series confirms that optimum hydrogen storage does not correspond to maximum defect density, but rather to a moderated and electronically active carbon framework. Our findings are also in excellent agreement with the computational predictions reported by Deniz et al. (2021). In the Li-doped fullerene-pillared graphene structure, the capacity increase arises from charge transfer due to binding of Li atoms to the fullerene/graphene framework and the associated induced-dipole-based physisorption mechanism. Positive centers formed around Li stabilize H_2 via multiple weak bonds; this electronic contribution works synergistically with the accessible pore network provided by fullerene pillars between graphene layers. At 77 K, where adsorption is governed by van der Waals interaction energy and confinement effects in micro/ultra-micropores, this synergy becomes particularly pronounced. As the doping level increases, the number of active adsorption centers initially rises and capacity increases; however, beyond a certain threshold, partial pore-blocking by Li reduces capacity, converting

electronic gains into geometric losses. Hence, while Li-induced polarization dominates at low–moderate filling, at higher filling levels the accessible pore network becomes the decisive factor, and capacity plateaus and then declines [50]. This transition from electronically controlled enhancement to geometrically limited adsorption explains the observed peak behavior and highlights the necessity of controlled Li incorporation rather than maximal doping.

Fig. 7 presents a proposed mechanism schematic showing that in D—C60 structures, hydrogen may be stored not only on the sphere surface but also in the interfacial regions between fullerene spheres and within external and internal voids. Defects are considered to create local vacancies and ring transformations, which can generate charge-density heterogeneities in the carbon framework and thus potentially provide favorable adsorption centers for hydrogen. When lithium is doped into these defect regions, Li atoms are proposed to preferentially interact with defective ends and edges, possibly forming electrostatically active Li^+ centers at which H_2 may adsorb via induced dipole–dipole interactions. In addition, Li species may also be partially distributed on the graphene surface and at graphene–fullerene interfacial regions, where they can contribute to local surface polarization and additional adsorption sites. Thus, hydrogen is suggested to interact not only with the carbon framework but also with the local electric fields around Li ions, which could lead to stronger but reversible adsorption. In nanocomposite systems, the intercalation of Li-doped defective fullerenes between graphene layers is proposed to increase the surface charge density while potentially widening the interlayer diffusion pathways, thereby creating additional pore channels that may become accessible to hydrogen. This structure is hypothesized to optimize the balance between electronic interaction (charge transfer) and geometric accessibility, which may explain the more pronounced capacity increase observed under cryogenic conditions. Similar to the findings of Ni et al. (2010) from a DFT-based study, Li doping of SWCNT enhances hydrogen storage primarily through an electronic polarization mechanism. Charge transfer from Li to the nanotube framework increases Li ionization and creates positive centers around Li, which bind H_2 more strongly yet reversibly through induced ion–dipole interactions. As the degree of positive charging increases, the H_2 binding energy rises and can reach ~0.26 eV in doubly charged systems, thereby providing a stable physisorption regime even near room temperature. Simultaneously, the increase in Li–nanotube binding energy with positive charge allows Li to remain more homogeneously dispersed without clustering, thereby increasing the number of effective adsorption centers. However, as the number of H_2 molecules coordinated to a single Li increases, the average binding energy per H_2 decreases due to local saturation of the polarization effect and the emergence of H_2–H_2 electrostatic interactions. In cases of excessive positive charge (e.g., loss of three electrons), system stability deteriorates and Li may detach from the surface; therefore, moderate positive charging and dispersed Li centers are preferred for optimal storage. Consequently, charge transfer in Li^+-doped SWCNT enhanced H_2 binding via Li^+ centers, induced dipole-based adsorption chain, and significantly increased the total storage capacity [53]. Similar findings were also reported in the theoretical work of Cho and Park (2007) on Li-doped single-walled carbon nanotubes (Li-SWCNTs). They showed that Li atoms bind to the nanotube surface and transfer electrons to the carbon lattice, generating positive Li^+ centers around the nanotube that adsorb H_2 molecules via induced dipole–dipole interactions. According to their calculations, relative to undoped SWCNTs, the binding energy increases by roughly an order of magnitude to ~ -4.5 kcal/mol, and each Li atom can adsorb on average $\sim 1.1H_2$ molecules. They also emphasized that a substantial share of the capacity arises not from the carbon surface itself but from electrostatic adsorption around Li^+ centers [54]. In sum, there is a strong parallel between the theoretical findings of Cho and Park [54] and the experimental observations in this study: Li doping reorganizes the electronic structure of carbon-based materials to create new active adsorption centers, thereby increasing the probability of hydrogen binding via polarizing interactions and significantly enhancing the total storage capacity.

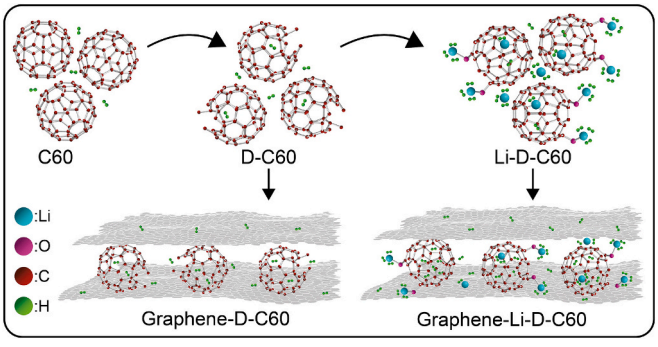

Fig. 7. The proposed adsorption mechanism of hydrogen on C60, D—C60, Li-D-C60, Graphene-D-C60 and Graphene-Li-D-C60.

In order to quantitatively evaluate the relationships between structural textural parameters and hydrogen storage performance, the experimental results obtained at cryogenic temperature (77 K) and approximately 100 bar were statistically analyzed using the Pearson correlation method. In this analysis, the hydrogen storage capacities of all hybrid samples were compared with their corresponding BET surface areas and micropore volumes. The correlation coefficients were found to be $r = 0.50$ for BET surface area and $r = 0.51$ for micropore volume, indicating a moderate positive relationship in both cases, though not statistically significant ($p > 0.05$). However, a very strong correlation was observed between BET surface area and micropore volume ($r = 0.99$), indicating pronounced collinearity between the textural parameters. Partial correlation analysis showed that, after controlling for micropore volume, the correlation between BET surface area and hydrogen storage nearly disappeared ($r \approx -0.02$), demonstrating that BET surface area is not an independent controlling factor. These results indicate that textural parameters provide a non-dominant contribution to hydrogen adsorption. Accordingly, hydrogen storage behavior is better explained by the cooperative influence of defect-induced adsorption sites, Li-related electronic polarization, and structural accessibility rather than by a single textural parameter. In particular, the Graphene-P2.5-Li-D-C60 sample exhibits the highest hydrogen uptake (2.53 wt%) despite having only an intermediate BET surface area (741 m^2/g), implying that electronic modulation and structural accessibility play cooperative roles. Overall, these findings confirm that hydrogen storage in the graphene/defective-fullerene/Li-doped hybrids is governed by a synergistic mechanism, in which accessible microporosity and Li-induced surface polarization collectively enhance adsorption efficiency rather than acting independently.

When the data in Table 4, are examined, it is observed that the hydrogen storage performance of carbon-based adsorbents varies significantly depending on the structural class of the material. For example, carbon spheres exhibit a hydrogen uptake of approximately 0.8 wt% at 77 K and 10 bar [12]. Under the same conditions, graphene-based materials typically show hydrogen storage capacities ranging from 0.52 to 1.20 wt%, depending on synthesis method and structural properties [14,55]. These variations have been attributed to differences in specific surface area, pore architecture, and defect density within the graphene framework. In Li-doped graphene systems, the capacity has been reported to increase to approximately 1.37 wt%, indicating that alkali metal doping can enhance adsorption through electronic interactions with hydrogen molecules [14]. Similarly, single-walled carbon nanotubes (SWCNTs) have been reported to exhibit hydrogen storage capacities of up to 1.46 wt% under identical conditions, highlighting the favorable adsorption behavior of high surface area carbon nanostructures [14]. However, Li-doped SWCNTs show a slightly lower capacity of approximately 1.32 wt%, suggesting that the effect of Li incorporation depends strongly on the structural environment of the carbon host [14]. In contrast, fullerene-based systems generally exhibit

Table 4
Excess hydrogen storage capacities of some carbon-derived adsorbents.

Samples	T (K)	P (bar)	H_2 wt%	References
Carbon sphere	77	10	0.8	[12]
Graphene	77	10	1.2	[55]
Li-doped graphene	77	10	1.37	[14]
SWCNT	77	10	1.46	[14]
D-C60	77	10	0.48	[15]
C70	77	10	0.04	[14]
Li-doped C70	77	10	0.32	[14]
Graphene	77	10	0.52	[14]
Schiff base based MWCNT	77	10	0.37	[57]
Li-D-C60	77	10	0.81	[27]
Li-doped SWCNT	77	10	1.32	[14]
MWCNT	77	10	0.52	[14]
Li-doped MWCNT	77	10	0.53	[14]
Activated carbon	77	10	1.88	[58]
Activated carbon	77	10	2.5	[60]
C60	77	10	0.21	[15]
MWCNT-COOH	77	10	0.5	[56]
Activated carbon	77	10	0.1	[60]
MWCNT-OH	77	10	0.5	[61]
Activated carbon	77	10	1.21	[48]
Graphene	77	10	0.95	In this study
Grapene-P1-D-C60	77	10	1.58	In this study
Graphene-P2.5-Li-D-C60	77	10	1.76	In this study

significantly lower hydrogen adsorption capacities. For example, pristine C60 has been reported to store approximately 0.21 wt% hydrogen at 77 K and 10 bar [15]. When structural defects are introduced into the fullerene framework, the capacity increases to about 0.48 wt% in defective C60 (D—C60), indicating that vacancy defects and structural distortions enhance adsorption sites [15]. Nevertheless, fullerene systems still remain relatively weak hydrogen adsorbents compared with other carbon nanostructures. For instance, C70 has been reported to exhibit a very low capacity of approximately 0.04 wt%, while Li-doped C70 shows a modest improvement to about 0.32 wt% [14]. These results collectively indicate that fullerene molecules alone do not provide sufficient adsorption sites or accessible surface area for efficient hydrogen storage. Multi-walled carbon nanotube (MWCNT) systems also show moderate hydrogen storage performance. Hydrogen adsorption capacities of approximately 0.52 wt% have been reported for pristine MWCNTs [14], while Li doping leads to only a marginal increase to 0.53 wt% [14]. Similarly, functionalized nanotube systems such as MWCNT-COOH and MWCNT-OH exhibit capacities of around 0.5 wt%, suggesting that surface functionalization alone does not necessarily result in substantial performance enhancement [56]. In Schiff-base functionalized MWCNT systems, the hydrogen adsorption capacity has been reported to be approximately 0.37 wt%, further indicating that chemical modification does not always translate into improved hydrogen storage behavior [57]. Among carbon-based adsorbents, activated carbon materials generally exhibit the highest hydrogen storage capacities, primarily due to their extremely high surface area and microporous structure. Hydrogen adsorption capacities of 0.1 wt%, 1.21 wt%, 1.88 wt%, and 2.5 wt% have been reported for different activated carbon systems under similar cryogenic conditions [48,58–60]. These results demonstrate the dominant role of microporosity and accessible surface area in determining hydrogen adsorption performance in porous carbon materials.

When the results obtained in the present study are evaluated under the same thermodynamic conditions, a notable enhancement in hydrogen storage performance is observed for the graphene–fullerene hybrid structures. In this work, pristine graphene exhibits a hydrogen storage capacity of 0.95 wt% at 77 K and 10 bar. When defective fullerene units are incorporated into the graphene matrix, the capacity increases to 1.58 wt% for the Graphene-P1-D-C60 sample. The highest hydrogen storage capacity is achieved in the Graphene-P2.5-Li-D-C60 sample, reaching 1.76 wt%. These values are higher than those reported for many graphene, nanotube, and fullerene systems investigated under identical experimental conditions [14,15,55–57]. A particularly noteworthy observation is that while fullerene phases alone exhibit relatively poor hydrogen storage performance, a significant enhancement is achieved when they are integrated within a graphene matrix. This improvement can be attributed to the structural and electronic synergy introduced by the hybrid architecture. Defective fullerene units can act as spacer structures between graphene layers, reducing restacking and preserving accessible microporosity. At the same time, Li incorporation introduces charge transfer and localized polarization centers, which enhance the interaction between hydrogen molecules and the carbon surface through induced dipole interactions. The simultaneous presence of these structural and electronic effects contributes to the improved hydrogen adsorption performance observed in the graphene/fulleren hybrid system. Overall, the comparative analysis performed under identical temperature and pressure conditions clearly indicates that Li-doped defective fullerene incorporated within a graphene matrix provides superior hydrogen storage performance compared with single-phase fullerene, graphene, and several carbon nanotube systems.

3.3. Adsorption isotherms

An adsorption isotherm is a curve that relates the gas pressure (P) to the equilibrium amount adsorbed (q_e) at constant temperature. It is therefore critical for identifying which mechanism or interaction dominates in an adsorption process (e.g., single- vs. multilayer uptake, homogeneous vs. heterogeneous adsorption sites, and the nature of adsorbate–surface/adsorbate–adsorbate interactions). In this study, the experimental data were analyzed by fitting the Freundlich, Langmuir, dual-Langmuir, Temkin and Toth isotherm models, using nonlinear regression in the original pressure–uptake domain without applying linearized transformations in order to avoid parameter bias. Model parameters were determined by minimizing the sum of squared errors (SSE) between experimental ($q_{e,exp}$) and calculated ($q_{e,cal}$) adsorption capacities, and the goodness of fit was assessed using the coefficient of determination (R^2).

The Freundlich isotherm is an empirical model for adsorption on heterogeneous surfaces, assuming non-uniform site energies. Its mathematical form is [14]:

$$q_e = k_F P^{1/n} \tag{1}$$

where q_e is the equilibrium uptake (mmol/g), P is the pressure (bar), k_F is a capacity-related constant (mmol/g $bar^{1/n}$), and n reflects surface heterogeneity.

The Langmuir isotherm describes monolayer adsorption on a homogeneous surface with identical, non-interacting sites, where each site binds one molecule and the uptake approaches a fixed saturation capacity. The Langmuir isotherm can be given in its nonlinear form as follows [48]:

$$q_e = \frac{q_m K_L P}{1 + K_L P} \tag{2}$$

where, q_e is the amount of adsorbate adsorbed (mmol/g); P is the pressure of the adsorbate (bar); q_m is the monolayer capacity (mmol/g); and K_L is the equilibrium constant (1/bar).

The dual-Langmuir isotherm assumes two types of adsorption sites with different energies and models uptake as the sum of two independent Langmuir terms. The isotherm equation is as follows [48]:

$$q_e = \frac{q_{m1} K_{L1} P}{1 + K_{L1} P} + \frac{q_{m2} K_{L2} P}{1 + K_{L2} P} \tag{3}$$

In this equation, q_{m1} and q_{m2} represent the maximum adsorption capacities of the two distinct site types (mmol/g), while K_{L1} and K_{L2} are denote their corresponding equilibrium constants (1/bar), reflecting different adsorption affinities.

The Temkin isotherm assumes a non-homogeneous surface where the adsorption energy varies linearly with surface coverage. The nonlinear form of this equation can be written as follows [14]:

$$q_e = B\ln(AP) \quad (4)$$

In this equation, A and B are Temkin constants, where A is related to the equilibrium binding constant (1/bar) and B is associated with the variation of adsorption energy (mmol/g).

The Toth isotherm is a semi-empirical model developed to describe adsorption on heterogeneous surfaces, particularly when deviations from the ideal Langmuir behavior are observed at intermediate and high pressures. The nonlinear form of the Toth equation is given as follows:

$$q_e = \frac{q_m K_T P}{\left(1 + (K_T P)^t\right)^{1/t}} \quad (5)$$

In this equation, q_m represent the maximum adsorption capacity (mmol/g), K_T is the Toth equilibrium constant (1/bar), and t is the heterogeneity parameter. When $t = 1$, Toth model reduces to the Langmuir isotherm [62].

The experimental hydrogen adsorption data were analyzed using the non-linear forms of the Freundlich, Langmuir, Temkin, Dual Langmuir, and Toth isotherm equations in the pressure range of 0–22 bar. The calculated isotherm parameters for each model, together with the corresponding correlation coefficients (R^2), are presented in Table 5. The use of direct non-linear regression rather than linearized transformations ensured a more reliable estimation of the model parameters and minimized error propagation associated with linearization procedures.

When the non-linear R^2 values are first considered, it is evident that although the Langmuir, Freundlich, and Temkin models provide a certain degree of agreement with the experimental data, the highest correlation coefficients are obtained for the Toth and Dual Langmuir models ($R^2 \approx 0.998$–0.999). This observation indicates that the hybrid graphene/fullerene systems cannot be fully described by a single-layer adsorption model assuming a homogeneous surface. Instead, the surface exhibits multiple adsorption energy levels. In this context, the Toth model accounts for surface energy heterogeneity, whereas the Dual Langmuir model represents the presence of two distinct adsorption regions. The high R^2 values therefore confirm that both models successfully capture the mathematical shape of the experimental isotherms. However, since R^2 does not penalize model complexity, it cannot be used alone for definitive model selection.

For this reason, Akaike Information Criterion (AIC) analyses were performed, and the results are presented in Table S.2 (Supplementery Materials). The AIC approach evaluates model performance by balancing goodness-of-fit against the number of adjustable parameters, thereby minimizing information loss. Examination of Table S.2 shows that the Langmuir, Freundlich, and Temkin models generally yield higher (less negative) AIC values and are therefore statistically less favorable. In contrast, the Toth and Dual Langmuir models provide the lowest AIC values. In some samples, the Dual Langmuir model exhibits a clear statistical advantage, while in others the Toth model provides the lowest AIC. Moreover, in several cases the ΔAIC between these two models is smaller than 2, indicating statistical equivalence.

Nevertheless, model selection should not rely solely on statistical indicators. The physical consistency between the calculated $q_{e,cal}$ values and the experimental adsorption capacities $q_{e,exp}$ must also be considered. In this regard, it is observed that the saturation capacities derived from the Toth model deviate significantly from the experimental values in certain samples. This deviation may arise from the sensitivity of the heterogeneity parameter at high pressure and from extrapolation effects when the adsorption plateau is not fully reached within the experimental range. In contrast, the sum of q_{m1} and q_{m2} obtained from the Dual Langmuir model shows better agreement with the experimental capacities and provides a more physically consistent interpretation.

The fact that the experimental data conform to the Dual Langmuir isotherm has important scientific implications. It suggests that the adsorption process does not occur on a uniform surface but instead involves two distinct adsorption sites or energy levels. The Dual Langmuir model assumes two independent adsorption mechanisms, each characterized by its own maximum capacity (q_{m1} and q_{m2}) and equilibrium constant (K_{L1} and K_{L2}). For graphene-based hybrid systems, this interpretation is physically meaningful. On one hand, hydrogen adsorption occurs on the extended sp^2 graphene surface via van der Waals interactions. On the other hand, defective fullerene units and/or Li-induced active centers introduce localized adsorption sites with different binding energies. Under cryogenic conditions, confinement effects within micro/ultra-micropores and Li-induced polarization interactions can coexist, further supporting the presence of two energetically distinct adsorption regions.

In conclusion, when non-linear R^2 analysis, AIC evaluation, and the physical consistency between calculated $q_{e,cal}$ and experimental $q_{e,exp}$ values are considered together, the results clearly indicate that the system cannot be described by a simple homogeneous adsorption model. Although both the Toth and Dual Langmuir models demonstrate strong

Table 5
Adsorption data calculated for adsorption of hydrogen on graphene and its nanocomposites.

Samples	$q_{e,exp}$ (mmol/g)	Langmuir			Freundlich	Temkin	Toth				Dual Langmuir				
		$q_m = q_{e,cal}$ (mmol/g)	K_L (1/bar)	R^2	R^2	R^2	$q_m = q_{e,cal}$ (mmol/g)	K_T (1/bar)	t	R^2	q_{m1} (mmol/g)	K_{L1} (1/bar)	q_{m2} (mmol/g)	K_{L2} (1/bar)	R^2
Graphene	5.533	6.379	0.25	0.9949	0.9751	0.8299	7.693	0.35	0.66	0.9991	1.00	2.39	5.77	0.15	0.9996
Graphene-P1-D-C60	8.648	8.508	0.94	0.9721	0.9801	0.9487	15.189	11.52	0.31	0.9993	3.26	11.30	6.44	0.23	0.9994
Graphene-P2.5-D-C60	7.249	7.445	0.74	0.9867	0.9759	0.9347	10.97	3.19	0.41	0.9988	2.07	11.33	6.04	0.30	0.9993
Graphene-P5-D-C60	8.144	8.108	0.93	0.9780	0.9800	0.9491	14.71	13.51	0.29	0.9991	2.54	23.27	6.43	0.30	0.9991
Graphene-P1-Li-D-C60	8.472	8.337	0.89	0.9721	0.9801	0.9521	15.711	12.08	0.29	0.9993	3.25	9.75	6.34	0.21	0.9994
Graphene-P2.5-Li-D-C60	9.688	9.529	0.89	0.9753	0.9824	0.9517	19.118	17.46	0.27	0.9994	3.32	15.76	7.45	0.24	0.9988
Graphene-P5-Li-D-C60	8.604	8.488	0.86	0.9764	0.9779	0.9668	15.365	9.67	0.31	0.9991	3.35	9.00	6.42	0.20	0.9992

statistical performance, the Dual Langmuir model provides superior physical interpretability and better agreement between calculated and experimental capacities. Therefore, it represents the most balanced and scientifically meaningful model for describing hydrogen adsorption in the investigated graphene/Li-D-C60 hybrid systems.

3.4. Adsorption kinetics

The interaction of hydrogen with carbon based materials, is an area of great interest due to its involvement in various areas of fundamental science and technology [63]. The rate at which graphene nanocomposites adsorb hydrogen gas indicates how rapidly the hydrogen gas reaches to this surface. Examining time-dependent adsorption q(t) profiles is critically important because it reveals not only the equilibrium capacity but also the dynamics of the process. As pressure increases, the q(t) curves for all samples attain higher values over time and the near-equilibrium plateau level rises markedly (Fig. 8). Experiments were carried out at 35, 42 and 70 bar at cryogenic temperature. For a given sample, profiles that are lower and more horizontal at low pressure become steeper at higher pressure and stabilize at a higher plateau; this systematic increase clearly demonstrates that the amount adsorbed increases with pressure. In the comparison across samples, the highest q(t) and plateau values are obtained for Graphene-P2.5-Li-D-C60, followed, in general, by Graphene-P1-D-C60. Graphene-P5-Li-D-C60 lies above pristine graphene at most pressures, Graphene-P5-D-C60 remains at an intermediate level, and Graphene-P2.5-D-C60 yields the lowest q(t) and plateau values within the series. This ordering indicates that, although the adsorbed amount increases with pressure for all samples, the hybrid architecture (D—C60 and Li-D-C60 loading level) meaningfully differentiates the plateau levels reached over time, with the highest performance achieved for Graphene-P2.5-Li-D-C60 formulation.

To investigate the adsorption kinetics and mechanism, the data were applied to the pseudo first-order (PFO), pseudo second-order (PSO), Elovich, Boyd, Weber-Morris, and Avrami equations. The equations and explanations related to these models are given in Table 6 [14,64–67]. The relevant graphs showing the highest regression coefficients from these models are given in Fig. S.3 (Supplementary Materials), and the data calculated from these graphs are shown in Table 7. The data in the Table 7 show that hydrogen adsorption is best described by PSO model at all pressures (35, 42 and 70 bar). The R^2 values obtained for the PSO model range from 0.9905 to 0.9979, providing the best fit across all sample–pressure combinations. In contrast, the PFO model systematically yields lower R^2 values (0.2785–0.7942), while the Elovich model, although mostly in the range of 0.7592–0.9362, exhibits a lower fitting performance than PSO. These results demonstrate that the q(t) curves are most consistently captured across the data set with the PSO assumptions, and that the PSO equation is the primary kinetic model for all samples. The strong fit to PSO indicates that the adsorption rate depends primarily on the occupancy of accessible surface sites (active sites); therefore, the process cannot be explained solely by the first-order exponential approximation (PFO) or Elovich-type activation due to covering alone. Furthermore, the $q_{e,cal}$ values calculated from PSO agree with the experimental $q_{e,exp}$ within a typical 2–7% deviation (e.g., 1.547 (exp)/1.510 mmol/g (cal) for graphene at 70 bar, 1.666/1.636 mmol/g for Graphene-P2.5-Li-D-C60, 1.705/1.730 mmol/g for Graphene-P2.5-D-C60). In addition, the PSO rate constant k_2 values are sensitive to the sample architecture and pressure; the general trend is that k_2 increases as the pressure decreases. Again, the comparison between the hydrogen adsorption amounts calculated at different pressure values using the PSO parameters and the experimental data is presented in Fig. 8. As can be seen, the fitted curves show an excellent agreement with the experimental results. A large body of kinetic studies reported in the literature on activated carbons [58], porous carbons [68], functionalized carbon nanotubes [61], and defect-engineered fullerenes [15] consistently demonstrates that hydrogen adsorption follows a pseudo-second-order kinetic model. These studies further highlight that this model effectively captures complex adsorption mechanisms involving multiple rate-limiting steps.

To investigate the adsorption mechanism of hydrogen on the surfaces of graphene and its nanocomposites, the experimental data were fitted using the Boyd, Weber–Morris, and Avrami equations, and the regression coefficients and the corresponding kinetic parameters calculated from these fitting curves are presented in Table 7. The results in Table 7 indicate that the H_2 uptake mechanism in the hybrid materials cannot be ascribed to a single rate-limiting step. The Boyd analysis yields generally low correlation coefficients ($R^2 \approx 0.2590$–0.5768), suggesting that adsorption kinetics cannot be explained solely by film or intraparticle diffusion, but rather proceed through a multi-step mechanism. The Weber–Morris evaluation quantitatively supports this interpretation: two linear regions are observed for all samples (Fig. 9). The first region shows high linearity with steep slopes ($R^2_1 = 0.8893$–0.9888; $k_{int1} > k_{int2}$), indicating that boundary-layer (film) diffusion dominates at the early stage, whereas the second region exhibits lower slopes and more moderate correlation coefficients ($R^2_2 \approx 0.1971$–0.8378), implying that intraparticle diffusion becomes rate-controlling as equilibrium is approached. As pressure decreases, the initial slope (k_{int1}) generally diminishes (e.g., for graphene, k_{int1} decreases from about 2.304 at 70 bar to 1.267 at 42 bar, and further to 0.991 at 35 bar), reflecting slower early-time uptake due to a reduced driving force; by contrast, some Li-containing hybrids retain relatively high initial accessibility at 70 bar, with $k_{int1} \approx 2.231$–2.424. In contrast, the Avrami model provides a relatively poor fit, with correlation coefficients typically ranging between 0.5887 and 0.9296 and n values below unity (≈0.261–0.510). Taken together, these results confirm that H_2 adsorption in the hybrid systems proceeds through a sequential, multi-step mechanism—boundary-layer effects dominate initially, while pore (intraparticle) diffusion becomes prominent near equilibrium. Consequently, performance optimization should focus on minimizing film resistance and tailoring pore architecture in an integrated manner.

4. Conclusion

The results obtained in this study clearly demonstrate that hydrogen adsorption in graphene/defective-fullerene/Li-doped hybrid nanocomposites proceeds via a multistep and reversible adsorption mechanism supported by diffusion and polarization effects. The introduction of vacancy defects into the fullerene structure increases the number and accessibility of energetically similar adsorption sites and nanopore channels, while also generating additional defect-associated adsorption environments within the hybrid carbon framework. This structural modification facilitates hydrogen diffusion toward the adsorption sites while preserving an efficient pore-accessible adsorption landscape. Subsequent Li doping at these defect sites generates localized surface polarization fields that strengthen H_2–surface interactions while maintaining a physisorption-dominated adsorption regime governed by van der Waals interactions. Graphene functions as a conductive and structural matrix that suppresses agglomeration, preserves slit-like porosity, and provides continuous and rapid diffusion pathways for hydrogen molecules.

Kinetic analyses confirm that hydrogen uptake follows a pseudo-second-order (PSO) rate law ($R^2 > 0.99$), indicating a surface-controlled adsorption process. Isotherm analyses further reveal that the adsorption equilibrium is best described by the dual-Langmuir model, suggesting the coexistence of two energetically distinguishable adsorption environments associated with defect-rich carbon regions and Li-polarized adsorption centers. The good agreement between the calculated adsorption capacities and experimental values confirms the physical consistency of the adsorption model. These findings indicate that the enhancement in hydrogen uptake originates primarily from an increased density of accessible adsorption centers and polarization-enhanced adsorption interactions rather than solely from surface energetic heterogeneity.

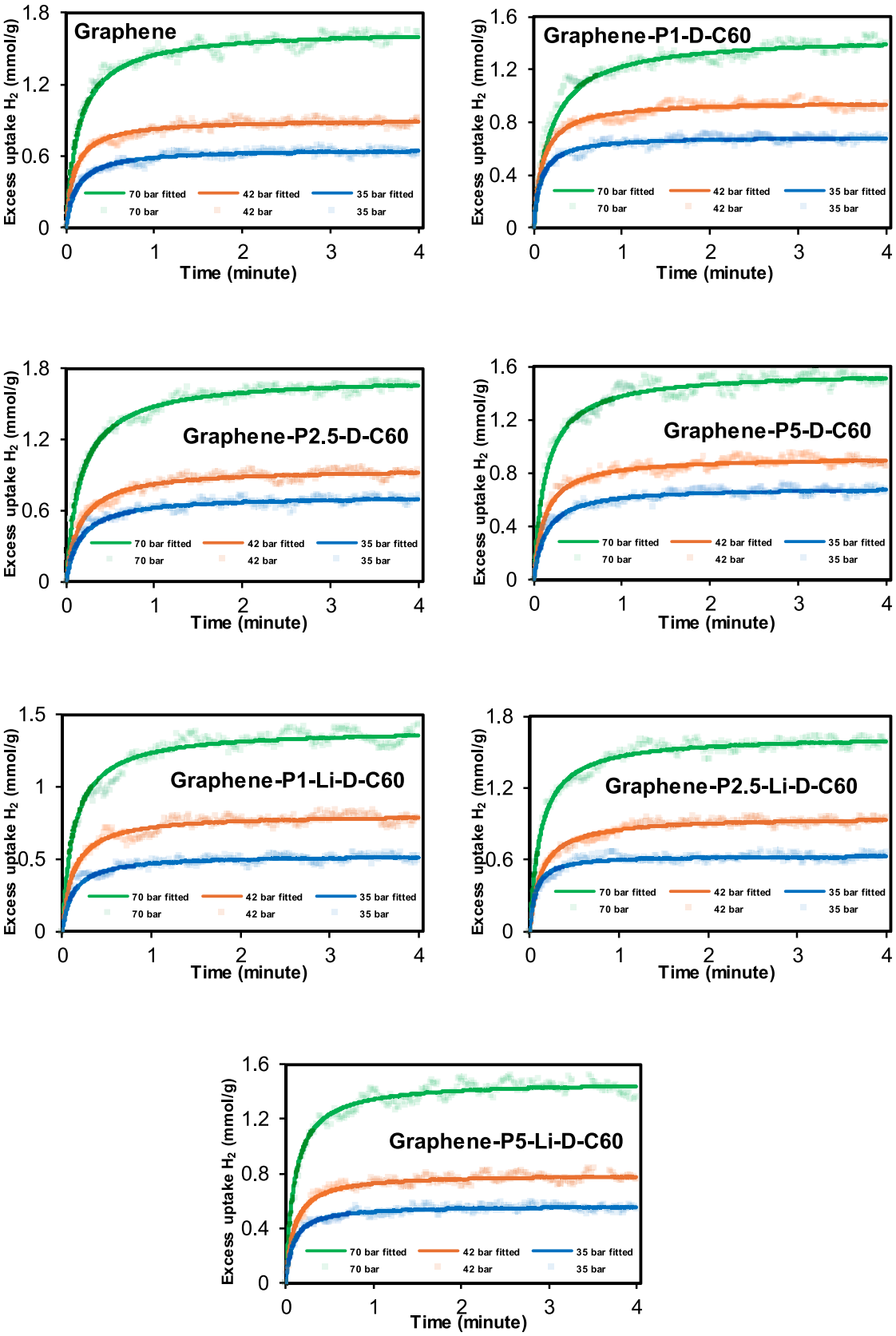

Fig. 8. The changing of adsorbed amounts with time for graphene and its nanocomposites at different pressures.

Table 6
Kinetic models and equations employed for the analysis of experimental data.

Kinetic models	Differential equation	Linearized form	Constants and units	References
Pseudo first-order	$\frac{dq_t}{dt} = k_1(q_e - q_t)$	$\ln(q_e - q_t) = lnq_e - k_1 t$	q_e and q_t are the amounts of adsorbed hydrogen (mmol/g) at equilibrium; t, time (min); k_1 is the pseudo-first-order rate constant (min^{-1})	[14]
Pseudo second-order	$\frac{dq_t}{dt} = k_2(q_e - q_t)^2$	$\frac{t}{q_t} = \frac{1}{k_2 q_e^2} + \frac{t}{q_e}$	k_2 is the pseudo-second-order kinetic rate constant (mmol/g min).	[14]
Elovich	$\frac{dq_t}{dt} = ae^{(-\beta q_t)}$	$q_t = \beta\ln(\alpha\beta) + \beta lnt$	α is the initial adsorption rate (mmol/g min) and β is a constant (g/mmol) related to the surface adsorption energy.	[64]
Boyd		$ln\left(1 - \frac{q_t}{q_e}\right) = -0.497 - \frac{\pi^2 D_c}{r_c^2} t$	q_t is the amount adsorbed at any time t (mmol/g); q_e is the amount adsorbed at equilibrium (mmol/g); D_c is the diffusion coefficient (cm^2/min); r_c is the diameter of the adsorbent (cm); t is the time (min).	[65]
Weber-Morris		$q_t = k_{int}\sqrt{t} + C$	k_{int} intraparticle diffusion rate constant (mmol/g $min^{1/2}$), C boundary layer effect (mmol/g).	[66]
Avrami	$q_t = q_e\left(1 - e^{-K_{Av}t^n}\right)$	$ln\left[-ln\left(1 - \frac{q_t}{q_e}\right)\right] = lnK_{Av} + nlnt$	n, an constant related to adsorption mechanism; K_{Av}: Avrami constant.	[67]

Table 7
Hydrogen adsorption kinetic data calculated from models of graphene nanocomposites.

Samples	P (bar)	First order R^2	Second order				Elovich	Boyd	Weber-Morris				Avrami		
			R^2	$q_{e,exp}$ (mmol/g)	$q_{e,cal}$ (mmol/g)	k_2 (mmol/g min)	R^2	R^2	R_1^2	k_{int1} (mol/g $min^{1/2}$)	R_2^2	k_{int2} (mol/g $min^{1/2}$)	R^2	n	K_{Av} (min^{-n})
Graphene	70	0.3433	0.9957	1.547	1.510	5.49	0.8638	0.4824	0.9888	2.304	0.7151	0.209	0.7654	0.427	1.91
	42	0.6892	0.9953	1.136	1.115	5.14	0.8660	0.5262	0.9616	1.267	0.6931	0.141	0.8430	0.419	1.74
	35	0.3818	0.9940	0.731	0.684	15.54	0.7592	0.3533	0.9798	0.991	0.3602	0.056	0.7057	0.361	1.75
Graphene-P1-D-C60	70	0.7831	0.9959	1.487	1.452	3.64	0.9137	0.5700	0.9854	1.857	0.8378	0.221	0.8991	0.425	1.63
	42	0.5347	0.9951	1.032	0.958	10.68	0.8389	0.4501	0.9553	1.311	0.5735	0.116	0.8053	0.342	1.70
	35	0.4132	0.9949	0.741	0.693	18.45	0.7785	0.3859	0.9543	0.921	0.3906	0.065	0.7254	0.320	1.85
Graphene-P2.5-D-C60	70	0.7942	0.9979	1.705	1.730	3.39	0.9362	0.5768	0.9734	1.878	0.7822	0.273	0.9296	0.510	1.92
	42	0.6336	0.9936	0.987	0.954	6.54	0.8898	0.5303	0.9615	1.146	0.6259	0.154	0.8588	0.443	1.65
	35	0.6419	0.9918	0.766	0.725	8.29	0.8700	0.5245	0.9676	0.927	0.6346	0.110	0.8389	0.398	1.56
Graphene-P5-D-C60	70	0.6161	0.9964	1.588	1.564	4.73	0.8629	0.4735	0.9756	2.427	0.6657	0.232	0.8377	0.441	1.89
	42	0.5593	0.9946	0.983	0.923	8.80	0.8364	0.4535	0.9778	1.326	0.6044	0.114	0.8036	0.376	1.65
	35	0.5732	0.9926	0.742	0.695	10.46	0.8601	0.4970	0.8893	0.830	0.5917	0.097	0.8155	0.387	1.58
Graphene-P1-Li-D-C60	70	0.5844	0.9944	1.494	1.398	5.37	0.8749	0.4864	0.9835	1.864	0.6212	0.230	0.8523	0.406	1.56
	42	0.5327	0.9925	0.861	0.810	9.64	0.8387	0.4595	0.9790	1.106	0.5855	0.118	0.7999	0.397	1.63
	35	0.5184	0.9905	0.560	0.526	15.24	0.7957	0.4313	0.9640	0.916	0.5540	0.072	0.7463	0.366	1.68
Graphene-P2.5-Li-D-C60	70	0.6216	0.9975	1.666	1.636	5.10	0.8671	0.4635	0.9810	2.424	0.6570	0.228	0.8568	0.432	1.93
	42	0.5539	0.9964	0.979	0.958	8.41	0.8736	0.4774	0.9836	1.326	0.6337	0.144	0.8385	0.439	1.88
	35	0.2785	0.9921	0.728	0.634	25.54	0.6483	0.2590	0.9555	0.998	0.1971	0.039	0.5887	0.261	1.56
Graphene-P5-Li-D-C60	70	0.5297	0.9955	1.629	1.474	6.94	0.8343	0.4167	0.9868	2.231	0.6068	0.185	0.8137	0.349	1.55
	42	0.4837	0.9942	0.908	0.796	13.22	0.7763	0.3676	0.9746	1.175	0.4488	0.069	0.7358	0.318	1.45
	35	0.4336	0.9935	0.618	0.565	21.42	0.7802	0.3861	0.9782	0.930	0.4965	0.063	0.7373	0.317	1.68

The Weber–Morris intraparticle diffusion model reveals two characteristic adsorption stages: an initial fast uptake dominated by boundary-layer (film) diffusion, followed by a slower intraparticle pore diffusion stage as equilibrium is approached. Boyd analysis demonstrates that no single rate-limiting step governs the entire adsorption process. Meanwhile, the Avrami model ($n < 1$) indicates a deceleratory kinetic profile consistent with diffusion-controlled adsorption kinetics. Taken together, these kinetic and diffusion analyses confirm that hydrogen uptake evolves through a sequential and cooperative mechanism, in which surface diffusion, intraparticle transport, and defect-induced polarization effects operate simultaneously.

The moderate Pearson correlation coefficients observed between hydrogen storage capacity and BET surface area ($r = 0.50$) or micropore volume ($r = 0.51$) indicate that adsorption performance cannot be explained solely by classical textural parameters. Instead, hydrogen uptake is governed by a synergistic interplay between pore accessibility, diffusion kinetics, and Li-induced electronic polarization. Accordingly, the optimized Graphene-P2.5-Li-D-C60 sample, achieving a hydrogen storage capacity of 2.53 wt% at 77 K and 100 bar, does not correspond to the highest BET surface area but rather represents the most favorable balance between geometric accessibility and polarization-enhanced binding strength.

In summary, hydrogen storage in these hybrid systems can be described as a dual-site physisorption process reinforced by defect-induced active site enrichment and dopant-driven polarization effects, with overall performance governed by the coordinated interaction between structural architecture, electronic modulation, and adsorption dynamics. This study establishes defect–dopant–matrix co-engineering as an effective and experimentally validated design strategy for carbon-based hydrogen adsorbents, providing a rational framework for the development of next-generation cryogenic hydrogen storage materials with tunable hybrid architectures.

CRediT authorship contribution statement

Yasemin Turhan: Writing – review & editing, Writing – original draft, Supervision, Methodology, Investigation, Conceptualization. **Betül Duman:** Methodology, Investigation. **Mehmet Doğan:** Writing –

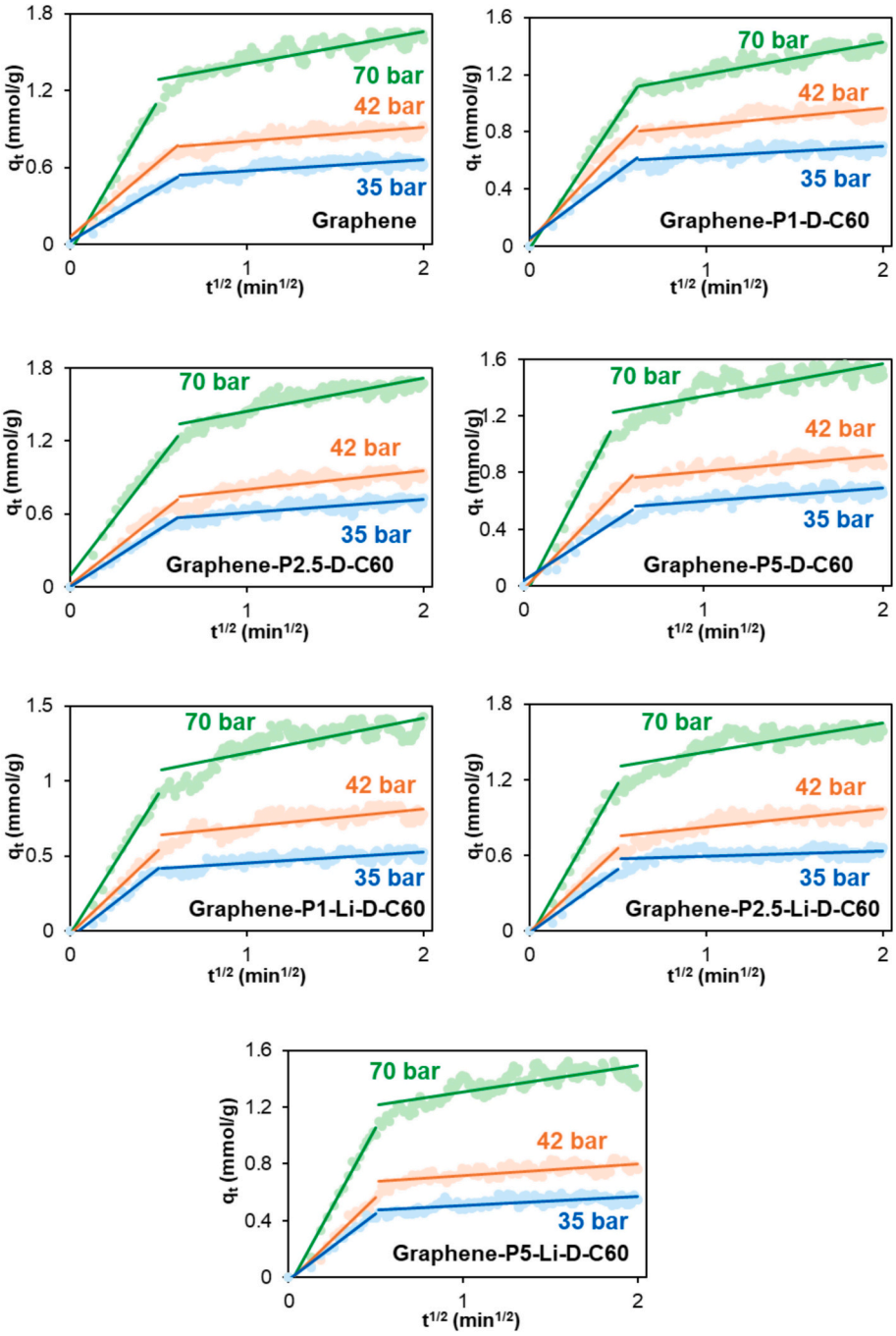

Fig. 9. The plots of q_t versus $t^{1/2}$ for Weber-Morris equation.

review & editing, Writing – original draft, Supervision, Software, Project administration, Methodology, Formal analysis, Data curation, Conceptualization. **Ersin Yanmaz:** Methodology, Investigation. **Zeynep Bicil:** Writing – original draft, Software, Methodology, Investigation, Data curation. **Berna Koçer Kızılduman:** Writing – review & editing, Writing – original draft, Software, Methodology, Investigation, Data curation.

Declaration of competing interest

The authors declare that they have no known competing financial interests or personal relationships that could have appeared to influence the work reported in this paper.

Acknowledgments

This work was supported by TUBİTAK (Project Number: 123Z536).

Appendix A. Supplementary data

Supplementary data to this article can be found online at https://doi.org/10.1016/j.cej.2026.175599.

Data availability

Data will be made available on request.

References

[1] S. Sgouridis, M. Carbajales-Dale, D. Csala, M. Chiesa, U. Bardi, Comparative net energy analysis of renewable electricity and carbon capture and storage, Nat. Energy 4 (6) (2019) 456–465.

[2] Y. Li, Q. Guo, Z. Ding, H. Jiang, H. Yang, W. Du, L.L. Shaw, MOFs-based materials for solid-state hydrogen storage: strategies and perspectives, Chem. Eng. J. 485 (2024) 149665.

[3] M. Hirscher, V.A. Yartys, M. Baricco, J.B. von Colbe, D. Blanchard, R. C. Bowman Jr., C. Zlotea, Materials for hydrogen-based energy storage–past, recent progress and future outlook, J. Alloys Compd. 827 (2020) 153548.

[4] S. Assyl, S. Botakoz, Z. Saule, Dimensions, structure, and morphology variations of carbon-based materials for hydrogen storage: a review, Discover Nano 20 (1) (2025) 115.

[5] O. Faye, J. Szpunar, U. Eduok, A critical review on the current technologies for the generation, storage, and transportation of hydrogen, Int. J. Hydrogen Energy 47 (29) (2022) 13771–13802.

[6] M. Murialdo, N.J. Weadock, Y. Liu, C.C. Ahn, S.E. Baker, K. Landskron, B. Fultz, High-pressure hydrogen adsorption on a porous electron-rich covalent organonitridic framework, ACS Omega 4 (1) (2019) 444–448.

[7] Z. Chen, K.O. Kirlikovali, K.B. Idrees, M.C. Wasson, O.K. Farha, Porous materials for hydrogen storage, Chem 8 (3) (2022) 693–716.

[8] L. Ouyang, K. Chen, J. Jiang, X.S. Yang, M. Zhu, Hydrogen storage in light-metal based systems: a review, J. Alloys Compd. 829 (2020) 154597.

[9] S. Wang, M. Gao, K. Xian, Z. Li, Y. Shen, Z. Yao, Y. Liu, H. Pan, $LiBH_4$ nanoconfined in porous hollow carbon nanospheres with high loading, low dehydrogenation temperature, superior kinetics, and favorable reversibility, ACS Appl. Energy Mater. 3 (4) (2020) 3928–3938.

[10] T. Thomas, S. Bontha, A. Bishnoi, P. Sharma, MXene as a hydrogen storage material? A review from fundamentals to practical applications, J. Energy Storage 88 (2024) 111493.

[11] A. Turkyilmaz, K. Isinkaralar, M. Dogan, B.K. Kizilduman, Z. Bicil, Production, characterization, and hydrogen storage properties of activated carbon from horse chestnut shell, Sustain. Chem. Pharm. 40 (2024) 101634.

[12] B.K. Kizilduman, Y. Turhan, M. Dogan, Mesoporous carbon spheres produced by hydrothermal carbonization from rice husk: optimization, characterization and hydrogen storage, Adv. Powder Technol. 32 (11) (2021) 4222–4234.

[13] F.N. Yalcinkaya, M. Dogan, Z. Bicil, B.K. Kizilduman, Effect of functionalization and Li-doping methods to hydrogen storage capacities of MWCNTs, Fuel 372 (2024) 132274.

[14] Z.S. Dogan, E.E. Dogan, Z. Bicil, B.K. Kizilduman, The effect of Li-doping and doping methods to hydrogen storage capacities of some carbonaceous materials, Fuel 396 (2025) 135280.

[15] M. Dogan, M.Y. Kalafat, B.K. Kizilduman, Z. Bicil, Y. Turhan, E. Yanmaz, B. Duman, Hydrogen storage analysis of fullerene and defective fullerenes: the first experimental study, Fuel 390 (2025) 134705.

[16] R. Ströbel, J. Garche, P.T. Moseley, L. Jörissen, G. Wolf, Hydrogen storage by carbon materials, J. Power Sources 159 (2) (2006) 781–801.

[17] M.J. Allen, V.C. Tung, R.B. Kaner, Honeycomb carbon: a review of graphene, Chem. Rev. 110 (1) (2010) 132–145.

[18] C.E.E. Rao, A.E. Sood, K.E. Subrahmanyam, A. Govindaraj, Graphene: the new two-dimensional nanomaterial, Angew. Chem. Int. Ed. 48 (42) (2009) 7752–7777.

[19] H. Chang, H. Wu, Graphene-based nanomaterials: synthesis, properties, and optical and optoelectronic applications, Adv. Funct. Mater. 23 (16) (2013) 1984–1997.

[20] K. Yang, L. Feng, X. Shi, Z. Liu, Nano-graphene in biomedicine: theranostic applications, Chem. Soc. Rev. 42 (2) (2013) 530–547.

[21] L.M. Veca, M.J. Meziani, W. Wang, X. Wang, F. Lu, P. Zhang, Y.P. Sun, Carbon nanosheets for polymeric nanocomposites with high thermal conductivity, Adv. Mater. 21 (20) (2009) 2088–2092.

[22] N. Kosar, M. Asgar, T. Mahmood, K. Ayub, H. Sajid, M.D. Albaqami, M.A. Gilani, Electrochemical properties of lithium metal doped C_{60} fullerene for battery applications, Mater. Sci. Semicond. Process. 175 (2024) 108256.

[23] A.A. El-Barbary, A.H. Shabi, Stone-Wales defective C_{60} fullerene for hydrogen storage, Int. J. Hydrogen Energy 71 (2024) 155–164.

[24] F. Wang, T. Zhang, X. Hou, W. Zhang, S. Tang, H. Sun, J. Zhang, Li-decorated porous graphene as a high-performance hydrogen storage material: a first-principles study, Int. J. Hydrogen Energy 42 (15) (2017) 10099–10108.

[25] I. Cabria, M.J. López, J.A. Alonso, Hydrogen storage in pure and Li-doped carbon nanopores: combined effects of concavity and doping, J. Chem. Phys. 128 (2008) 144704.

[26] M. Pumera, Graphene-based nanomaterials for energy storage, Energ. Environ. Sci. 4 (2011) 668–674.

[27] Y. Turhan, B. Duman, M. Doğan, E. Yanmaz, Z. Bicil, B. Koçer Kızılduman, Enhanced hydrogen storage in lithium-doped defective fullerenes: experimental optimization, adsorption mechanisms, and kinetic–isotherm modeling, Diamond Relat. Mater. 163 (2026) 113399.

[28] A.K. Akhila, P.S. Vinitha, N.K. Renuka, Photocatalytic activity of graphene–titania nanocomposite, Mater. Today Proc. 5 (8) (2018) 16085–16093.

[29] J. Yan, Z. Zhao, L. Pan, Growth and characterization of graphene by chemical reduction of graphene oxide in solution, Phys. Status Solidi A 208 (10) (2011) 2335–2338.

[30] R. Katiyar, D.S. Bag, I. Nigam, Synthesis and evaluation of swelling characteristics of fullerene (C_{60}) containing cross-linked poly(2-hydroxyethyl methacrylate) hydrogels, Adv. Mater. Lett. 5 (4) (2014) 214–222.

[31] G. Peng, L.L. Zhang, X.L. Yang, S. Duan, G. Liang, Y.H. Huang, Enhanced electrochemical performance of multi-walled carbon nanotubes modified Li2FeSiO4/C cathode material for lithium-ion batteries, J. Alloys Compd. 570 (2013) 1–6.

[32] R.O. Loutfy, S. Katagiri, Fullerene materials for lithium-ion battery applications, in: Perspectives of Fullerene Nanotechnology, Springer Netherlands, Dordrecht, 2002, pp. 357–367.

[33] J.A. Teprovich Jr., M.S. Wellons, R. Lascola, S.J. Hwang, P.A. Ward, R.N. Compton, R. Zidan, Synthesis and characterization of a lithium-doped fullerane (Li x-C60-H y) for reversible hydrogen storage, Nano Lett. 12 (2) (2012) 582–589.

[34] C.U. Deniz, H. Mert, C. Baykasoglu, Li-doped fullerene pillared graphene nanocomposites for enhancing hydrogen storage: a computational study, Comput. Mater. Sci. 186 (2021) 110023.

[35] W. Yan-Wei, L. Hui-Jun, P. Lu, T. Xiao-Jian, S. Jing, First-principles study of Li doping in a double-wall carbon nanotube, Chin. Phys. Lett. 26 (8) (2009) 087102.

[36] Y.W. Wen, H.J. Liu, L. Miao, Y. Hu, Theoretical study of alkali atom doped outside 4 Å carbon nanotubes, J. Nanosci. Nanotechnol. 10 (8) (2010) 5399–5403.

[37] N. Bendiab, E. Anglaret, J.L. Bantignies, A. Zahab, J.L. Sauvajol, P. Petit, C. Mathis, S. Lefrant, Stoichiometry dependence of the Raman spectrum of alkali-doped single-wall carbon nanotubes, Phys. Rev. B 64 (24) (2001) 245424.

[38] B. Kartick, S.K. Srivastava, Green synthesis of graphene, J. Nanosci. Nanotechnol. 13 (6) (2013) 4320–4324.

[39] C. Akinyi, J.O. Iroh, Thermal decomposition and stability of hybrid graphene–clay/polyimide nanocomposites, Polymers 15 (2) (2023) 299.

[40] F. Farivar, P.L. Yap, R.U. Karunagaran, D. Losic, Thermogravimetric analysis (TGA) of graphene materials: effect of particle size of graphene, graphene oxide and graphite on thermal parameters, C 7 (2) (2021) 41.

[41] F. Farivar, P.L. Yap, K. Hassan, T.T. Tung, D.N. Tran, A.J. Pollard, D. Losic, Unlocking thermogravimetric analysis (TGA) in the fight against "fake graphene" materials, Carbon 179 (2021) 505–513.

[42] Y. Pan, Z. Guo, S. Ran, Z. Fang, Influence of fullerenes on the thermal and flame-retardant properties of polymeric materials, J. Appl. Polym. Sci. 137 (1) (2020) 47538.

[43] G. Lisa, C.I. Cleminte, T. Michinobu, Thermal stability and degradation mechanism of C_{60} fullerene-based polymers, J. Appl. Polym. Sci. 141 (11) (2024) e55079.

[44] D. Radevych, M. Gajdardziska-Josifovska, C.J. Hirschmugl, M. Weinert, Interaction of lithium with a monolayer of graphene monoxide, J. Phys. Chem. C 125 (22) (2021) 11820–11827.

[45] D. Wijerathne, Y. Gong, S. Afroj, N. Karim, C. Abeykoon, Mechanical and thermal properties of graphene nanoplatelets-reinforced recycled polycarbonate composites, Int. J. Lightweight Mater. Manuf. 6 (1) (2023) 117–128.

[46] G. Wang, J. Yang, J. Park, X. Gou, B. Wang, H. Liu, J. Yao, Facile synthesis and characterization of graphene nanosheets, J. Phys. Chem. C 112 (22) (2008) 8192–8195.

[47] D.P. Hansora, N.G. Shimpi, S. Mishra, Graphite to graphene via graphene oxide: an overview on synthesis, properties, and applications, JOM 67 (12) (2015) 2855–2868.

[48] P.T. Beyli, M. Dogan, Z. Bicil, Y. Turhan, E. Yanmaz, B.K. Kizilduman, Hydrogen storage performance of sunflower stalk-derived activated carbons produced via $ZnCl_2$ and KOH activation, Energy Storage 7 (6) (2025) e70260.

[49] M. Thommes, K. Kaneko, A.V. Neimark, J.P. Olivier, F. Rodriguez-Reinoso, J. Rouquerol, K.S. Sing, Physisorption of gases, with special reference to the evaluation of surface area and pore size distribution (IUPAC technical report), Pure Appl. Chem. 87 (9–10) (2015) 1051–1069.

[50] C.U. Deniz, H. Mert, C. Baykasoglu, Li-doped fullerene pillared graphene nanocomposites for enhancing hydrogen storage: a computational study, Comput. Mater. Sci. 186 (2021) 110023.

[51] M.A. De la Casa-Lillo, F. Lamari-Darkrim, D. Cazorla-Amoros, A. Linares-Solano, Hydrogen storage in activated carbons and activated carbon fibers, J. Phys. Chem. B 106 (42) (2002) 10930–10934.

[52] M. Rzepka, P. Lamp, M.A. De la Casa-Lillo, Physisorption of hydrogen on microporous carbon and carbon nanotubes, J. Phys. Chem. B 102 (52) (1998) 10894–10898.

[53] M. Ni, L. Huang, L. Guo, Z. Zeng, Hydrogen storage in Li-doped charged single-walled carbon nanotubes, Int. J. Hydrogen Energy 35 (8) (2010) 3546–3549.

[54] J.H. Cho, C.R. Park, Hydrogen storage on Li-doped single-walled carbon nanotubes: computer simulation using the density functional theory, Catal. Today 120 (3–4) (2007) 407–412.

[55] G. Srinivas, Y. Zhu, R. Piner, N. Skipper, M. Ellerby, R. Ruoff, Synthesis of graphene-like nanosheets and their hydrogen adsorption capacity, Carbon 48 (3) (2010) 630–635.

[56] M. Dogan, A. Selek, O. Turhan, B.K. Kizilduman, Z. Bicil, Different functional groups functionalized hexagonal boron nitride (h-BN) nanoparticles and multi-walled carbon nanotubes (MWCNT) for hydrogen storage, Fuel 303 (2021) 121335.

[57] Ü. Çakır, F. Kestel, B.K. Kizilduman, Z. Bicil, M. Dogan, Multi-walled carbon nanotubes functionalized by hydroxyl and Schiff base and their hydrogen storage properties, Diamond Relat. Mater. 120 (2021) 108604.

[58] Y. Turhan, M.B. Yeşilbiçer, B.K. Kizilduman, M. Doğan, Z. Bicil, Cryogenic hydrogen storage on peanut shell-derived activated carbons: isotherm, kinetics and mechanism, J. Energy Storage 140 (2025) 118998.

[59] K. Isinkaralar, G. Gullu, A. Turkyilmaz, M. Dogan, O. Turhan, Activated carbon production from horse chestnut shells for hydrogen storage, Int. J. Global Warming 26 (4) (2022) 361–373.

[60] E.E. Doğan, P. Tokcan, B.K. Kızılduman, Storage of hydrogen in activated carbons and carbon nanotubes, Adv. Mater. Sci. 18 (4) (2018) 5–16.

[61] Z. Bicil, Adsorption kinetics and mechanism of hydrogen on pristine and functionalized multi-walled carbon nanotubes, Fuel 403 (2026) 136130.

[62] J. Serafin, B. Dziejarski, O.F. Cruz Junior, J. Sreńscek-Nazzal, Design of highly microporous activated carbons based on walnut shell biomass for H_2 and CO_2 storage, in: Carbon vol. 201, 2023, pp. 633–647.
[63] V.V. Ivanovskaya, A. Zobelli, D. Teillet-Billy, N. Rougeau, V. Sidis, P.R. Briddon, Hydrogen adsorption on graphene: a first principles study, Eur. Phys. J. B. 76 (3) (2010) 481–486.
[64] W. Rudzinski, T. Panczyk, Kinetics of isothermal adsorption on energetically heterogeneous solid surfaces: a new theoretical description based on the statistical rate theory of interfacial transport, J. Phys. Chem. B 104 (39) (2000) 9149–9162.
[65] E.W.E. Shahrin, N.A.H. Narudin, N.N.M. Shahri, M. Nur, J.W. Lim, M.R. Bilad, A. H. Mahadi, J. Hobley, Usman, A comparative study of adsorption behavior of rifampicin, streptomycin, and ibuprofen contaminants from aqueous solutions onto chitosan: dynamic interactions, kinetics, diffusions, and mechanisms, Emerg. Contam. 9 (1) (2023) 100199.
[66] K.H. Chu, M.A. Hashim, M.H. Zawawi, J.C. Bollinger, The Weber–Morris model in water contaminant adsorption: Shattering long-standing misconceptions, J. Environ. Chem. Eng. 13 (4) (2025) 117266.
[67] H. Qiu, L. Lv, B.C. Pan, Q.J. Zhang, W.M. Zhang, Q.X. Zhang, Critical review in adsorption kinetic models, J. Zhejiang Univ. Sci. A 10 (5) (2009) 716–724.
[68] M. Karadaş, G. Duman, M. Doğan, Y. Turhan, T. Karayıldırım, Hydrogen storage performance of porous carbons from waste cotton: activation strategies, isotherm and kinetic analyses, Fuel 409 (2026) 137820.